Gaussian-Markovian quantum Fokker-Planck approach to nonlinear spectroscopy and wavepacket dynamics for a dissipative molecular system

Yutaka Maruyama

Doctor of Philosophy

Department of Functional Molecular Science
School of Mathematical and Physical Science
The Graduate University for Advanced Studies

August 14, 1998

ABSTRACT

Quantum coherence and its dephasing by coupling to a dissipative environment play an important role in time-resolved nonlinear optical response as well as noadiabatic transitions in the condensed phase. Nonlinear optical processes of a multi-state one-dimensional system with Morse potential in a dissipative environment were discussed. This was based on a numerical study using the multi-state quantum Fokker-Planck equation for a colored Gaussian-Markovian noise bath, which was expressed as a hierarchy of kinetic equations. This equation can treat strong system-bath interactions at a low temperature, where quantum effects play a major role. The approach applies to linear absorption measurements as well as pump-probe and photon echo spectroscopy. Laser induced photo dissociation and predissociation were studied for the potential of Cs_2. Nuclear wavepackets were calculated in the Wigner representation and compared with femtosecond pump-probe spectroscopy for various displacements of potentials and heat-bath parameters. The pump-probe spectra show the dependence of displacement and exhibit dissociation and predissociation dynamics. We demonstrated that the photon echo signals can detect the effect of anharmonicity of potential surface as broadening of peaks. Numerical calculations of probe absorption spectra for strong pump pulse were also presented and discussed. The results show dynamical Stark splitting, but, in contrast to the Bloch equations which contain an infinite-temperature dephasing, we found that at finite temperature their peaks have different heights even when the pump pulse is on

resonance. Furthermore we observed effect of the diabatic coupling between excited and dissociative states as peaks on spectra.

Acknowledgements

I could not have gotten to this point without help. First of all I would like to thank my research advisor, Professor Yoshitaka Tanimura, for all of his guidance and encouragement.

I would also like to express my sincere appreciation to Professor Shaul Mukamel for his helpful guidance and comments during my stay at University of Rochester.

Numerous members of the theoretical research groups in Institute for Molecular Science have been helpful as well, and I owe them thanks.

The numerical calculations were performed at the computer center of Institute for Molecular Science.

Contents

Chapter 1

General Introduction

Most chemical reactions take place in a condensed phase, such as a liquid state environment[1]. It is therefore not surprising that scientists have a great interest in the exploration of the dynamics in the condensed phase. Such system is, however, relatively difficult to understand because the system is disturbed from the environment. For example linear absorption measurements provide information on the energetics; however, this information is often obscured by the broad linewidths at room-temperature.

The developments in the generation of ultrafast laser pulses, with pulse durations close to the typical vibrational period of molecular vibrations[2], have led to a situation that nonlinear ultrafast spectroscopic measurements can now easily be conducted. The absorption and emission spectrum of the dissolved probe are characterized by broad and structureless bands, but the nonlinear optical spectroscopies provide us with a wealth of information about the physical system being studied, and may allow the experimentalist to overcome the problems of environment-induced obscurities of the signal. Furthermore, ultrafast nonlinear optical experiments give us information regarding relaxation timescales, which is not available from ordinary absorption experiment for a dissipative system.

In the last decade, many nonlinear optical effects have been explored in studies of nuclear dynamics in condensed phases, and it was shown that each technique projects onto certain types of molecular motion. For instance, while the optical Kerr effect probes solvent motions associated with anisotropic Raman polarizabilities, far-infrared spectroscopy only senses dipolar molecular motions, while optical

absorption and emission spectroscopies cover all molecular motions that couple to optical transition.

Optical spectroscopic techniques differ in the characteristics of the excitation fields applied to the sample. Generally two classes can be defined, the time domain and the frequency domain spectroscopy. In the time domain experiments the temporal duration of the excitation pulse can be regarded as short on the timescales of the dynamics of the system, which is on the order of tens or hundreds of femtoseconds. Spectrally this is equivalent to the condition that the spectrum of the excitation source exceeds the linewidth of the relevant optical transition. The selectivity of probing the dynamics in the time domain, relaxes the particular sensitivity in the spectral domain. Different classes of time domain experiments such as pump-probe[3, 4, 5] and photon echo[6, 7, 8] spectroscopy have been used to investigate the problem of dynamics for a dissipative system. The frequency domain experiments distinguish themselves by their selectivity in the frequency domain. Inherently to the spectral sensitivity, temporal resolution is relaxed. Also in the frequency domain, the techniques such as picosecond CARS[9] and absorption/emission[10] spectroscopy have been applied as probes of a condensed phase system as well.

The time domain and the frequency domain spectroscopies are complementary in terms of their sensitivity with respect to time scale and it is therefore essential to consider both domains in order to acquire a complete picture of dynamics of the system. While Fourier-transform relations exist both for linear and nonlinear optical susceptibilities, time domain optical experiments have the possibility of creating a

time-window through which molecular motion can be explored[11]. In this thesis various time domain nonlinear optical methods are studied to unravel the optical dynamics of a dissipative system.

The understanding of such highly resolved measurements demands theoretical descriptions which go far beyond simple models. A tremendous insight has been gained by comparing qualitative arguments, quantitative analytical calculations[15, 16], and numerical studies[17, 18, 19, 20, 21] with experiments. By using the multimode Brownian oscillator or spin-boson Hamiltonian, a phenomenological description of molecular motions in condensed phase has been investigated theoretically[12, 13]. The response function approach[22], which is based on a perturbative expansion of the optical polarization in powers of the laser fields, has been successfully applied to study four-wave[12, 23], and six-wave mixing experiments[24, 25]. Calculation of the response functions involves integration over the nuclear degrees of freedom. Thus, one could obtain the response function only for a system with harmonic potential surfaces. It is possible to include any coordinate dependence of transition dipole moments on coordinates (non-Condon effects) or a weak anharmonicity into the Nth-order response function by using a nonequilibrium generating functional, which is obtained by the path-integral approach[15, 16, 26]. Applicability of this approach is, however, still limited.

To investigate the nonlinear optical process one can also use wavepacket representation[14]. With ultrashort pulses one can now prepare a molecular wavepacket and probe its evolution and observe molecular reactions in the time domain[27, 28]. For a long

time the wavepacket had no real practical use because their generation seemed impossible. However, recent advances in the physics and chemistry of laser interactions with atoms and molecules have brought actual wavepacket in experiments. The experimental work on femtosecond excitation and the observation of the subsequent wavepacket dynamics are quite extensive and reviewed recently. For example, it became possible to prepare wavepacket by exciting atoms to Rydberg states with short pulses[29].

One of the major reasons for studying wavepacket dynamics of a molecule is the possibility of enhancing, or controlling chemical reactions by careful application of pulses of light with optimal frequency, intensity, duration, and timing[30, 31, 32]. A simple example, which can be called 'controlled', is the photodissociation of a molecule theoretically. Here new products are formed by using a light pulse to transfer a stable ground state wavepacket to an unstable dissociative potential. In a recent experiment, controlling over the dissociation of NaI was demonstrated[33]. Another approach is using multi pulses of light. A typical problem is to overcome a barrier on the ground state potential and this is achieved in two steps. The method can be generalized to overcome barriers on excited states and the concepts of control theory can be used to design optimally shaped light pulses to produce the desired products[34, 35].

The femtosecond timescale often allows one to exclude the spontaneous decay of the excited state population by calculations. However, in the processes following the excitation it can play a role and it may interfere with the excitation process

itself. There is a related problem in the treatment of molecular system in the condensed phase, which neglected the effect of environment. In general Shrödinger equation can't contain the effect of heat bath, but one can treat the dissipation by using quantum Fokker-Planck equation. The quantum kinetic equation for reduced density matrix elements can treat arbitrary potential surface and shape of laser field. In this thesis we study various optical processes by calculating time-evolution of wavepacket.

In the remainder of thesis we shall consider nonlinear spectroscopy for a dissipative system by using multistate quantum Fokker-Planck equation for a Gaussian-Markovian noise bath. In the next chapter, we describe the model Hamiltonian for a dissipative system and present the multi-state quantum Fokker-Planck equation. Chapter 3 presents the procedure for calculating the absorption, pump-probe and impulsive two pulse photon echo spectrum. In Chapter 4, we calculate the linear absorption, pump-probe spectra and two-pulse photon echo signals for various displacement and heat-bath parameters. The spectra show the effect of heat bath and displacement. Chapter 5 is devoted to concluding remarks. We explain the possibilities of quantum Fokker-Planck approach.

Chapter 2

Method of Calculation

Y. Tanimura and Y. Maruyama,

"Gaussian-Markovian quantum Fokker-Planck approach to nonlinear spectroscopy of a displaced Morse potentials system: Dissociation, predissociation, and optical Stark effects",

J. Chem. Phys. 107 (1997) 1779.

Y. Maruyama and Y. Tanimura,

"Pump-probe spectra and nuclear dynamics for a dissipative molecular system in a strong laser field: predissociation dynamics",

Chem. Phys. Lett. 292 (1998) 28.

2.1 Introduction

Optical processes can be calculated using a direct integration of the equations of motion in the presence of fields. By calculating the relevant wave function or density matrix elements, it becomes possible to explore optical processes for a system with arbitrary potential surfaces. A difficulty with this approach is the proper treatment of dephasing processes induced by a heat bath. These can be incorporated using equations of motion for a reduced density matrix, such as the quantum master equation or the quantum Fokker-Planck equation. Effects of the bath are then taken into account by introducing a damping operator, which can be obtained by assuming Gaussian-white noise fluctuations and a bilinear system-bath interaction expressed as $H_{SB} = R\sum c_n x_n = \sum c_n(a^+ + a^-)(b_n^+ + b_n^-)$, where $a^\pm$ and $b_n^\pm$ are the creation and annihilation operators corresponding to the system and the bath coordinates, respectively. We should notice that the reduced density matrix equation with the bilinear interaction can be applied only to the high temperature system, i.e., $\hbar\omega_c/k_BT \ll 1$, where ω_c is the characteristic frequency of the system. If one applies these equations beyond this limitation, then one obtains unphysical results such as the negative probability of density matrix elements. For the master equation, this phenomenon is known as breaking of dynamic positivity[36], which is the limit of the reduced equation of motion approach. If one modifies an interaction in the resonant form (or the rotating wave approximation form), i.e., $H'_{SB} = \sum c_n(a^+b_n^- + a^-b_n^+)$ then this temperature limitation can be relaxed. We should notice, however, that

this modification of the Hamiltonian alters the dynamics described by the original Hamiltonian, though the obtained equation of motion can be applied to the low temperature system. The neglect of the off-resonant terms $a^- b_n^- + a^+ b_n^+$ can be systematically performed by using the averaging method for the generalized master equation before taking the long-time (white-noise) limit.

We can relax this temperature limitation without modifying H_{SB} by employing the colored Gaussian-Markovian noise bath instead of the Gaussian-white noise bath. The time correlation function of noise fluctuation, $\Omega(t)$, in the Gaussian-white noise is expressed as $< \Omega(t)\Omega(t') >= \delta(t-t')$, whereas $< \Omega(t)\Omega(t') >= \exp[-\gamma(t-t')]$ in the Gaussian-Markovian case. If the characteristic time scale of the system, $1/\omega_c$, is much longer than the correlation time of noise, $\tau = 1/\gamma$, then one may regard the noise as the δ function in t. In the present case of femtosecond experiments, however, the noise must be treated as a finitely correlated function of time. Thus, the generalization to the Gaussian-Markovian is also requirements of describing a system in the realistic condition.

We could obtain a hierarchy of kinetic equations for reduced density matrices which can describe the system interacting with the colored Gaussian-Markovian noise bath[37]. Physically, one can think of this hierarchy of equations as dealing with a set of density matrices modeling the various numbers of phonons excited states in very special way. This equation was originally obtained for a discrete two-level system, and can be regarded as a generalization of the quantum master equation. We then showed that a similar hierarchy of kinetic equations could be

obtained for a system in the coordinate representation, which can be regarded as a generalization of the quantum Fokker-Planck equation[38, 39]. In principle, we can choose any representation to describe quantum dynamics of a system. Practically, however, the coordinate representation has some advantages to study a system with anharmonic potential surfaces. First, the coordinate description allows us to make direct interpretations of the dynamics. Thus, we may easily discuss the classical and the quantum systems on the same basis. Second, we can suppress the open boundary conditions, where the wavepacket can go out from the edge of potential. In the discrete state representation, the eigenstates become continuous for an open boundary system, which makes impossible to integrate the equation of motion. Thus, if one has to deal with the problem with the open boundary such that the problem of photo dissociation, one needs to adapt the coordinate space representation. Third, calculations are easier. One has to calculate a number of eigenstates and eigen energies to describe a system in the discrete state representation. Various interactions, such as laser interactions and the system-bath interactions are then expressed as matrices in this basis. Such calculations are computationally intensive except for a system with harmonic potential surfaces. In the coordinate representation, we can avoid such calculations for any shape of potentials and interactions.

The quantum Fokker-Planck equation was originally aiming to study a single potential surface system. By a simple and straightforward generalization, we can derive the multi-state quantum Fokker-Planck equation to apply to a system with multi-potential surfaces.[40]

2.2 Multi-State Quantum Fokker-Planck Equation for a Gaussian-Markovian Noise Bath

First we consider a diatomic molecular system. Here we assume the molecular structure allows the following approximation: the Born-Oppenheimer approximation[41, 42], in which it is supposed that the nuclei, being so much heavier than electron, move relatively slowly and may be treated as stationary while the electrons move relative to them. We can therefore think of the nuclei as being fixed at an arbitrary relative coodinate, and then solve the Shrödinger equation for the wavefunction of the electrons for the nuclear separation. Then we can choose a different separation and repeat the calculation, and so on. In this way we can explore how the energy of the molecule varies with bond length, and obtain a molecular potential energy curve. It is called a potential energy curve because the kinetic energy of the nuclei is zero as they are stationary. The Born-Oppenheimer treatment yields adiabatic energy curves which do not cross if they are of the same symmetry. An alternative representation involves diabatic surfaces that can cross. Diabatic surfaces preserve the dominant characteristics of the electronic wave functions, but the surfaces have non-zero interaction matrix elements which control the rate of trasition from one surface to the other. The diabatic basis is a unitary transformation of the adiabatic electronic basis.

Then we employ the electronic states denoted by $|j>$, and the Hamiltonian of

the system is expressed as

$$H_S = \frac{p^2}{2M} + \sum_{j,k} |j > U_{jk}(q) < k|. \tag{2.1}$$

Here, q is a nuclear coordinate strongly coupled to the electronic state and p is its conjugate momentum. The diagonal element $U_{jj}(q)$ is the potential surface of the jth electronic surface, and the off-diagonal element $U_{jk}(q)$ with $j \neq k$ represents the diabatic coupling between the jth and kth states. In the laser spectroscopy experiment the system interacts with the laser fields, then the Hamiltonian in the rotating wave approximation is expressed by

$$H_A^0(t) = H_S + \sum_{l=1}^{n} E_l(t)(e^{ik_l r - i\Omega_l t}\mu_l^+ + e^{-ik_l r + i\Omega_l t}\mu_l^-), \tag{2.2}$$

where $E_l(t)$ are the temporal envelopes of the laser pulses, and $\mu_l^+ = \mu|e >< g|$ and $\mu_l^- = \mu|g >< e|$ are the dipole operators of molecular system. In the Hamiltonian (2.2) we have made the dipole approximation, thus neglecting the interaction of higher-order multipoles with the electromagnetic field.

The multi-state density matrix for the Hamiltonian Eq. (2.2) may be expanded in the electronic basis set as

$$\hat{\rho}(t) = \sum_{j,k} |j > \rho_{jk}(q_L, q_R; t) < k|. \tag{2.3}$$

Here, $\rho_{jk}(q_L, q_R; t)$ is expressed in the coordinate representation.

We assume that the primary nuclear coordinate is coupled to a bath which is represented by a set of harmonic oscillators with frequencies ω_n, masses m_n, coordinates q_n and momenta p_n. The interaction between the system and the nth

oscillator is assumed to be linear with a coupling strength c_n. The total Hamiltonian is then given by [43]

$$H_A(t) = H_A^0(t) + H'. \tag{2.4}$$

where

$$H' = \sum_n \left[\frac{p_n^2}{2m_n} + \frac{m_n\omega_n^2}{2}\left(q_n - \frac{c_n q}{m_n\omega_n^2}\right)^2 \right]. \tag{2.5}$$

Character of the heat-bath is specified by the spectral distribution: All information about the bath which is required for a reduced description of the system dynamics, is contained in its initial temperature and its spectral density

$$J(\omega) \equiv \omega \sum_n \left(\frac{c_n^2}{4m_n\omega_n^2}\right)(\delta(\omega-\omega_n) + \delta(\omega+\omega_n)). \tag{2.6}$$

The function $J(\omega)$ is related to the symmetric correlation function of a collective bath coordinate ($X = \sum c_n x_n$),

$$\frac{1}{2} < X(t)X + XX(t) >= \hbar \int d\omega J(\omega) \coth\left(\frac{\beta\hbar\omega}{2}\right)\cos(\omega t), \tag{2.7}$$

where $\beta = 1/k_B T$ is the inverse temperature of the bath, and the time evolution of X is determined by the pure bath Hamiltonian (Eq. (2.5) with $q = 0$). Here $< \cdots >$ denotes $tr\{e^{-\beta H}\cdots\}/tr\{e^{-\beta H}\}$. We assume an Ohmic dissipation with the Lorentzian cutoff,

$$J(\omega) = \frac{M\zeta}{2\pi}\frac{\omega\gamma^2}{\gamma^2+\omega^2}. \tag{2.8}$$

With the assumption of the high temperature bath $\beta\hbar\omega \leq 1$, this spectral density represents a Gaussian-Markovian noise where the symmetric correlation function of

the noise induced by the heat bath, is given by

$$\frac{1}{2} < X(t)X + XX(t) >= \frac{M\zeta\gamma}{\beta} e^{-\gamma t}. \tag{2.9}$$

Thus, ζ and γ correspond to the friction and the relaxation time of the noise, respectively. In this case, one can trace over the heat-bath degrees of freedom and obtain the equation of motion in the hierarchy form [37, 38, 39]. The important point is that restriction for condition does not involve the system frequencies (which can be small or large compared to β^{-1}), but only a high temperature requirement with respect to the bath, which is much easier to meet. For the nth member of hierarchy, $\rho_{jk}^{(n)}$, where j and k represent diabatic states, the equation of motion is expressed as[40]

$$\begin{aligned} i\hbar\frac{\partial}{\partial t}\rho_{jk}^{(0)}(q_L, q_R; t) = & - \frac{\hbar^2}{2M}\left(\frac{\partial^2}{\partial q_L^2} - \frac{\partial^2}{\partial q_R^2}\right)\rho_{jk}^{(0)}(q_L, q_R; t) \\ & + [U(q_L) - U(q_R)]\rho_{jk}^{(0)}(q_L, q_R; t) \\ & + (q_L - q_R)\rho_{jk}^{(1)}(q_L, q_R; t), \end{aligned} \tag{2.10}$$

$$\begin{aligned} i\hbar\frac{\partial}{\partial t}\rho_{jk}^{(1)}(q_L, q_R; t) = & - \frac{\hbar^2}{2M}\left(\frac{\partial^2}{\partial q_L^2} - \frac{\partial^2}{\partial q_R^2}\right)\rho_{jk}^{(1)}(q_L, q_R; t) \\ & + [U(q_L) - U(q_R)]\rho_{jk}^{(1)}(q_L, q_R; t) \\ & - i\hbar\gamma\rho_{jk}^{(1)}(q_L, q_R; t) + (q_L - q_R)\rho_{jk}^{(2)}(q_L, q_R; t) \\ & + \frac{\hbar^2\zeta\gamma}{2}\left(\frac{\partial}{\partial q_L} - \frac{\partial}{\partial q_R}\right)\rho_{jk}^{(0)}(q_L, q_R; t) \\ & + \frac{\zeta\gamma M}{\beta}(q_L - q_R)\rho_{jk}^{(0)}(q_L, q_R; t), \end{aligned} \tag{2.11}$$

and

$$
\begin{aligned}
i\hbar\frac{\partial}{\partial t}\rho_{jk}^{(n)}(q_L,q_R;t) = & - \frac{\hbar^2}{2M}\left(\frac{\partial^2}{\partial q_L^2}-\frac{\partial^2}{\partial q_R^2}\right)\rho_{jk}^{(n)}(q_L,q_R;t) \\
& + [U(q_L)-U(q_R)]\rho_{jk}^{(n)}(q_L,q_R;t) \\
& - in\hbar\gamma\rho_{jk}^{(n)}(q_L,q_R;t)+(q_L-q_R)\rho_{jk}^{(n+1)}(q_L,q_R;t) \\
& + \frac{n\hbar^2\zeta\gamma}{2}\left(\frac{\partial}{\partial q_L}-\frac{\partial}{\partial q_R}\right)\rho_{jk}^{(n-1)}(q_L,q_R;t) \\
& + \frac{n\zeta\gamma M}{\beta}(q_L-q_R)\rho_{jk}^{(n-1)}(q_L,q_R;t), \qquad (2.12)
\end{aligned}
$$

where ζ is the friction constant. The hierarchy elements of reduced density matrix $\rho_{jk}^{(n)}$ are defined in the path integral form[38, 39]. The equation of motion is derived by performing time derivative of these hierarchy elements. This hierarchy of equations handle a set of reduced density matrix, modeling the states of the system with various numbers of phonons excited in the bath. In this formulation, $\rho_{jk}^{(0)}$ includes all order of the system-bath interaction and is the exact solution for the Hamiltonian Eq. (2.4). Then $\rho_{jk}^{(1)}$, $\rho_{jk}^{(2)}$, ..., $\rho_{jk}^{(n)}$ describe the distribution functions with a smaller set of the system-bath interaction, corresponding to the complete set of the system-bath interactions minus 1st, 2nd, ..., nth order of the system-bath interaction, respectively. Thus, one can think that this formulation takes the opposite direction to the conventional perturbative expansion approaches, where the zeroth member does not include any system-bath interaction, then the first, second, third, etc, members gradually take into account the higher-order interactions and approach to the exact solution. We shall be interested only in the zeroth member of the hierarchy $\rho_{jk}^{(0)}$ which is identical to ρ_{jk} defined in Eq.(2.5). The other elements

$n \neq 0$ are not related to the physical observable and introduced for computational purposes. For the element of large hierarchy number $N\gamma \gg \omega_c$ where ω_c is the characteristic frequency of the system such as the frequency of the harmonic potential, the above hierarchy can be terminated by[38]

$$\begin{aligned} i\hbar\frac{\partial}{\partial t}\rho_{jk}^{(N)}(q_L,q_R;t) = & -\frac{\hbar^2}{2M}\left(\frac{\partial^2}{\partial q_L^2}-\frac{\partial^2}{\partial q_R^2}\right)\rho_{jk}^{(N)}(q_L,q_R;t) \\ & + [U(q_L)-U(q_R)]\rho_{jk}^{(N)}(q_L,q_R;t) \\ & - iN\hbar\gamma\rho_{jk}^{(N)}(q_L,q_R;t) \\ & - \frac{i\hbar\zeta}{2}(q_L-q_R)\left(\frac{\partial}{\partial q_L}-\frac{\partial}{\partial q_R}\right)\rho_{jk}^{(N)}(q_L,q_R;t) \\ & - \frac{i\zeta M}{\beta\hbar}(q_L-q_R)(q_L-q_R)\rho_{jk}^{(N)}(q_L,q_R;t) \\ & + \frac{N\hbar^2\zeta\gamma}{2}\left(\frac{\partial}{\partial q_L}-\frac{\partial}{\partial q_R}\right)\rho_{jk}^{(N-1)}(q_L,q_R;t) \\ & + \frac{N\zeta\gamma M}{\beta}(q_L-q_R)\rho_{jk}^{(N-1)}(q_L,q_R;t), \end{aligned} \tag{2.13}$$

Using this hierarchal structure we may deal with strong system-bath interactions in addition to a colored noise. In the white noise limit $\gamma \gg \omega_c$ we may terminate the hierarchy of Eqs. (2.10)-(2.13) by setting $N = 0$, obtaining the multi-state quantum Fokker-Planck equation for a Gaussian- white noise bath:

$$\begin{aligned} i\hbar\frac{\partial}{\partial t}\rho_{jk}(q_L,q_R;t) = & -\frac{\hbar^2}{2M}\left(\frac{\partial^2}{\partial q_L^2}-\frac{\partial^2}{\partial q_R^2}\right)\rho_{jk}(q_L,q_R;t) \\ & + [U(q_L)-U(q_R)]\rho_{jk}(q_L,q_R;t) \\ & - \frac{i\hbar\zeta}{2}(q_L-q_R)\left(\frac{\partial}{\partial q_L}-\frac{\partial}{\partial q_R}\right)\rho_{jk}(q_L,q_R;t) \\ & - \frac{i\zeta M}{\beta\hbar}(q_L-q_R)(q_L-q_R)\rho_{jk}(q_L,q_R;t), \end{aligned} \tag{2.14}$$

If we consider a system with a single potential surface, then the above equation further reduces to the quantum Fokker-Planck equation that was obtained by Caldeira and Leggett[44]. Since we have assumed $\beta\hbar\gamma \leq 1$, the temperature limitation of the Gaussian-white case is more stringent than the Gaussian-Markovian case.

We can switch to the Wigner (phase space) representation[45, 46, 47, 48, 49]

$$W_{jk}(P,R;t) = \frac{1}{2\pi\hbar}\int_{-\infty}^{\infty} dr e^{iPr/\hbar}\rho_{jk}(R-r/2, R+r/2;t). \tag{2.15}$$

and the density matrix may then be written as

$$W(t) = \sum_{j,k} |j> W_{jk}(P,R;t) < k|. \tag{2.16}$$

The Wigner representation has the following advantages; first it allows us to compare the quantum density matrix directly with its classical counterpart. Second, using phase space distribution functions, we can further easily impose the necessary boundary conditions (e.g. periodic or open boundary conditions), where particles can move in and out of the system. This is much more difficult in the coordinate representation. Third, in the numerical calculation the Wigner representation requires less memory than the coordinate representation, because the number of grid for momentum need not as large as that for position.

In the Wigner representation the equation of motion is given by [40]

$$\begin{aligned}\frac{\partial}{\partial t}W^{(0)}_{jk}(P,R;t) = & - \frac{P}{M}\frac{\partial}{\partial R}W^{(0)}_{jk}(P,R;t) \\ & - \frac{1}{\hbar}\int\frac{dP'}{2\pi\hbar}\sum_m [X_{jm}(P-P',R;t)W^{(0)}_{mk}(P',R;t) \\ & + X^*_{mk}(P-P',R;t)W^{(0)}_{jm}(P',R;t)]\end{aligned}$$

$$+ \quad \frac{\partial}{\partial P} W_{jk}^{(1)}(P,R;t), \tag{2.17}$$

$$\begin{aligned}
\frac{\partial}{\partial t} W_{jk}^{(1)}(P,R;t) = & - \frac{P}{M}\frac{\partial}{\partial R} W_{jk}^{(1)}(P,R;t) \\
& - \frac{1}{\hbar}\int \frac{dP'}{2\pi\hbar} \sum_m [X_{jm}(P-P',R;t) W_{mk}^{(1)}(P',R;t) \\
& + X_{mk}^{*}(P-P',R;t) W_{jm}^{(1)}(P',R;t)] \\
& - \gamma W_{jk}^{(1)}(P,R;t) + \frac{\partial}{\partial P} W_{jk}^{(2)}(P,R;t) \\
& + \zeta\gamma \left(P + \frac{M}{\beta}\frac{\partial}{\partial P}\right) W_{jk}^{(0)}(P,R;t),
\end{aligned} \tag{2.18}$$

$$\begin{aligned}
\frac{\partial}{\partial t} W_{jk}^{(n)}(P,R;t) = & - \frac{P}{M}\frac{\partial}{\partial R} W_{jk}^{(n)}(P,R;t) \\
& - \frac{1}{\hbar}\int \frac{dP'}{2\pi\hbar} \sum_m [X_{jm}(P-P',R;t) W_{mk}^{(n)}(P',R;t) \\
& + X_{mk}^{*}(P-P',R;t) W_{jm}^{(n)}(P',R;t)] \\
& - n\gamma W_{jk}^{(n)}(P,R;t) + \frac{\partial}{\partial P} W_{jk}^{(n+1)}(P,R;t) \\
& + n\zeta\gamma \left(P + \frac{M}{\beta}\frac{\partial}{\partial P}\right) W_{jk}^{(n-1)}(P,R;t),
\end{aligned} \tag{2.19}$$

and anchor equation for large N

$$\begin{aligned}
\frac{\partial}{\partial t} W_{jk}^{(N)}(P,R;t) = & - \frac{P}{M}\frac{\partial}{\partial R} W_{jk}^{(N)}(P,R;t) \\
& - \frac{1}{\hbar}\int \frac{dP'}{2\pi\hbar} \sum_m [X_{jm}(P-P',R;t) W_{mk}^{(N)}(P',R;t) \\
& + X_{mk}^{*}(P-P',R;t) W_{jm}^{(N)}(P',R;t)] \\
& - N\gamma W_{jk}^{(N)}(P,R;t) + \zeta\frac{\partial}{\partial P}\left(P + \frac{M}{\beta}\frac{\partial}{\partial P}\right) W_{jk}^{(N)}(P,R;t) \\
& + N\zeta\gamma \left(P + \frac{M}{\beta}\frac{\partial}{\partial P}\right) W_{jk}^{(N-1)}(P,R;t).
\end{aligned} \tag{2.20}$$

Here,

$$X_{ij}(P,R;t) = i\int dr e^{iPr/\hbar}U_{ij}(R-r/2;t) \tag{2.21}$$

and

$$X^{*}_{ij}(P,R;t) = -i\int dr e^{iPr/\hbar}U_{ij}(R+r/2;t) \tag{2.22}$$

are the Fourier transform representation of the potential terms which are convenient for studying the quantum effects.

In a similar way the multi-state quantum Fokker-Planck equation for a Gaussian white noise bath is expressed as

$$\begin{aligned}\frac{\partial}{\partial t}W^{(0)}_{jk}(P,R;t) = &- \frac{P}{M}\frac{\partial}{\partial R}W^{(0)}_{jk}(P,R;t)\\ &- \frac{1}{\hbar}\int\frac{dP'}{2\pi\hbar}\sum_m[X_{jm}(P-P',R;t)W^{(0)}_{mk}(P',R;t)\\ &+ X^{*}_{mk}(P-P',R;t)W^{(0)}_{jm}(P',R;t)]\\ &+ \zeta\frac{\partial}{\partial P}\left(P+\frac{M}{\beta}\frac{\partial}{\partial P}\right)W^{(0)}_{jk}(P,R;t).\end{aligned} \tag{2.23}$$

In the numerical calculation, we employed the dimensionless coordinate and momentum defined by $r \equiv R\sqrt{M\omega_0/\hbar}$ and $p \equiv P\sqrt{1/M\hbar\omega_0}$, respectively, where ω_0 is the system characteristic frequency. Then the equation of motion is expressed as

$$\begin{aligned}\frac{\partial}{\partial t}W^{(0)}_{jk}(p,r;t) = &- \omega_0 p\frac{\partial}{\partial r}W^{(0)}_{jk}(p,r;t)\\ &- \frac{1}{\hbar}\int\frac{dp'}{2\pi}\sum_m[X_{jm}(p-p',r;t)W^{(0)}_{mk}(p',r;t)\\ &+ X^{*}_{mk}(p-p',r;t)W^{(0)}_{jm}(p',r;t)]\\ &+ \omega_0\frac{\partial}{\partial p}W^{(1)}_{jk}(p,r;t),\end{aligned} \tag{2.24}$$

$$\begin{aligned}\frac{\partial}{\partial t}W_{jk}^{(1)}(p,r;t) = &- \omega_0 p\frac{\partial}{\partial r}W_{jk}^{(1)}(p,r;t)\\ &- \frac{1}{\hbar}\int\frac{dp'}{2\pi}\sum_m[X_{jm}(p-p',r;t)W_{mk}^{(1)}(p',r;t)\\ &+ X_{mk}^*(p-p',r;t)W_{jm}^{(1)}(p',r;t)]\\ &- \gamma W_{jk}^{(1)}(p,r;t) + \omega_0\frac{\partial}{\partial p}W_{jk}^{(2)}(p,r;t)\\ &+ \frac{\zeta\gamma}{\omega_0}\left(p+\frac{1}{\beta\hbar\omega_0}\frac{\partial}{\partial p}\right)W_{jk}^{(0)}(p,r;t),\end{aligned} \tag{2.25}$$

$$\begin{aligned}\frac{\partial}{\partial t}W_{jk}^{(n)}(p,r;t) = &- \omega_0 p\frac{\partial}{\partial r}W_{jk}^{(n)}(p,r;t)\\ &- \frac{1}{\hbar}\int\frac{dp'}{2\pi}\sum_m[X_{jm}(p-p',r;t)W_{mk}^{(n)}(p',r;t)\\ &+ X_{mk}^*(p-p',r;t)W_{jm}^{(n)}(p',r;t)]\\ &- n\gamma W_{jk}^{(n)}(p,r;t) + \omega_0\frac{\partial}{\partial p}W_{jk}^{(n+1)}(p,r;t)\\ &+ \frac{n\zeta\gamma}{\omega_0}\left(p+\frac{1}{\beta\hbar\omega_0}\frac{\partial}{\partial p}\right)W_{jk}^{(n-1)}(p,r;t),\end{aligned} \tag{2.26}$$

$$\begin{aligned}\frac{\partial}{\partial t}W_{jk}^{(N)}(p,r;t) = &- \omega_0 p\frac{\partial}{\partial r}W_{jk}^{(N)}(p,r;t)\\ &- \frac{1}{\hbar}\int\frac{dp'}{2\pi}\sum_m[X_{jm}(p-p',r;t)W_{mk}^{(N)}(p',r;t)\\ &+ X_{mk}^*(p-p',r;t)W_{jm}^{(N)}(p',r;t)]\\ &- N\gamma W_{jk}^{(N)}(p,r;t) + \zeta\frac{\partial}{\partial p}\left(p+\frac{1}{\beta\hbar\omega_0}\frac{\partial}{\partial p}\right)W_{jk}^{(N)}(p,r;t)\\ &+ \frac{N\zeta\gamma}{\omega_0}\left(p+\frac{1}{\beta\hbar\omega_0}\frac{\partial}{\partial p}\right)W_{jk}^{(N-1)}(p,r;t).\end{aligned} \tag{2.27}$$

and

$$\begin{aligned} X_{ij}(p,r;t) &= i\int dr' e^{ipr} U_{ij}(r-r'/2;t), \\ X^{*}_{ij}(p,r;t) &= -i\int dr' e^{ipr} U_{ij}(r+r'/2;t). \end{aligned} \tag{2.28}$$

2.3 Bath Coodinate Representation

In this section, we present another representation of quantum Fokker-Planck equation for a Gaussian-Markovian noise bath. The multi-state density matrix for the Hamiltonian Eq. (2.1) may be expanded in the electronic basis set as

$$\hat{\rho}(t) = \sum_{j,k} |j> \rho_{jk}(q_L, q_R, \Omega; t) < k|. \tag{2.29}$$

Here, $\rho_{jk}(q_{L,}, q_R, \Omega; t)$ is expressed in the coordinate representation, which includes bath coordinate Ω. The system-bath dynamics is described by evolution of wavepackets $\rho_{ij}(q_L, q_R, \Omega; t)$. The equation of motion has the form [50]

$$\begin{aligned} i\hbar\frac{\partial}{\partial t}\rho_{jk}(q_L,q_R,\Omega;t) &= -\frac{1}{2M}\left(\frac{\partial^2}{\partial q_L^2} - \frac{\partial^2}{\partial q_R^2}\right)\rho_{jk}(q_L,q_R,\Omega;t) \\ &+ [V_j(q_L) - V_k(q_R)]\rho_{jk}(q_L,q_R,\Omega;t) \\ &+ i\gamma\frac{\partial}{\partial\Omega}\left(\Omega + \sigma\frac{\partial}{\partial\Omega}\right)\rho_{jk}(q_L,q_R,\Omega;t) \\ &- \Omega(q_L - q_R)\rho_{jk}(q_L,q_R,\Omega;t) \\ &+ \frac{1}{2}\zeta\gamma\left(\frac{\partial}{\partial q_L} - \frac{\partial}{\partial q_R}\right)\frac{\partial}{\partial\Omega}\rho_{jk}(q_L,q_R,q;t), \end{aligned} \tag{2.30}$$

where

$$\sigma = M\zeta\lambda k_B T. \tag{2.31}$$

Here Ω represents collective bath coordinate, which contains the effect of the bath. The bath coordinate Ω can be regarded as the Stochastic variable in the Kubo's stocastic Liouville equation[51]. Equation (2.29) is thus idential to the stochastic equation of motion obtained by Tanimura and Kubo (Eq. (4.25)) of [37], although here we exress the equation in the oordinate space. We can also treat the system coupled to the Gaussian-Markovian noise bath by using this equation.

In the Wigner (phase space) representation

$$W_{jk}(P,R,\Omega;t)=\frac{1}{2\pi\hbar}\int_{-\infty}^{\infty}dre^{iPr/\hbar}\rho_{jk}(R-r/2,R+r/2,\Omega;t), \tag{2.32}$$

and the density matrix may then be written as

$$W(t)=\sum_{j,k}|j><W_{jk}(P,R,\Omega;t)<k|. \tag{2.33}$$

The equation of motion is given by

$$\begin{aligned}\frac{\partial}{\partial t}W_{jk}(p,r,\Omega';t)= &-\omega_0 p\frac{\partial}{\partial r}W_{jk}(p,r,\Omega';t)\\ &-\frac{1}{\hbar}\int\frac{dP'}{2\pi\hbar}\sum_m[X_{jm}(p-p',r,\Omega';t)W_{mk}(p,r,\Omega';t)\\ &+X^*_{mk}(p-p',r;t)W_{jm}(p',r,\Omega';t)]\\ &+\gamma\frac{\partial}{\partial\Omega'}\left(\Omega'+\frac{\partial}{\partial\Omega'}\right)W_{jk}(p,r,\Omega';t)\\ &-\sqrt{\frac{\zeta\gamma k_BT}{\hbar\omega_0}}\Omega'\frac{\partial}{\partial p}W_{jk}(p,r,\Omega';t)\\ &+\sqrt{\frac{\hbar\omega_0\zeta\gamma}{k_BT}}p\frac{\partial}{\partial\Omega'}W_{jk}(p,r,\Omega';t),\end{aligned} \tag{2.34}$$

where we have introduced the dimensionless coordinate and momentum defined by $r\equiv R\sqrt{M\omega_0/\hbar}$, $p\equiv P\sqrt{1/M\hbar\omega_0}$ and $\Omega'\equiv\Omega\sqrt{\sigma}$, respectively.

We may deal with strong system-bath interactions in addition to a colored noise by using this Ω bath representation.

Chapter 3

Linear and Nonlinear Spectroscopy

Y. Tanimura and Y. Maruyama,

"Gaussian-Markovian quantum Fokker-Planck approach to nonlinear spectroscopy of a displaced Morse potentials system: Dissociation, predissociation, and optical Stark effects",

J. Chem. Phys. 107 (1997)1779.

Y. Maruyama and Y. Tanimura,

"Pump-probe spectra and nuclear dynamics for a dissipative molecular system in a strong laser field: predissociation dynamics",

Chem. Phys. Lett. 292 (1998) 28.

3.1 Linear Absorption and Pump-Probe Spectroscopy

In a pump-probe experiment, the molecular system is prepared by a first laser pulse (the "pump") into a nonstationary state, the time evolution of which is probed by a time-delayed second laser pulse (the "probe"). In the impulsive pump limit, in which the duration of the pump is much shorter than the nuclear dynamics timescale, vibronic motions in phase space may result in coherent oscillations (its quantum beats). In most pump-probe experiments only the energy of the probe pulse is measured. By dispersing the probe pulse, having a broad spectrum, in a spectrograph after it has passed through the sample, one can achieve high-resolution time-dependent absorption and dispersion spectra. [52, 53]

We consider a molecular system with electronic states strongly coupled to a single nuclear coordinate. The Hamiltonian is expressed by Eq. (2.1). In this chapter, we study a linear and nonlinear spectroscopy in a multi-level system with Morse potential surfaces[54] denoted by $|g>$, $|e>$, $|e'>$ and $|f>$.(Fig. 3.1) The transition frequency between g and e and between e and f are denoted by ω_{ge} and ω_{ef}. We assume that the system is initially in the ground equilibrium state $\rho_g=|g>\rho_g<g|$, where ρ_g is the equilibrium distribution function of the ground potential surface. In a pump-probe experiment, the system subjected to two light pulses: with frequencies and wave vectors are Ω_1, k_1 and Ω_2, k_2, respectively. We assume that the carrier frequency of the pump laser Ω_1 is close to the electronic transition frequency between g and e. The probe frequency Ω_2 is chosen to (i) $\Omega_2 \approx \omega_{ge}$ for a measurement

between g and e, and (ii) $\Omega_2 \approx \omega_{ef}$ for a measurement between e and f. The total Hamiltonian is then given by

$$\begin{aligned} H_A(t) = H_S &+ E_1(t)(e^{i\mathbf{k_1}\mathbf{r}-i\Omega_1 t}\mu_1^+ + e^{-i\mathbf{k_1}\mathbf{r}+i\Omega_1 t}\mu_1^-) \\ &+ E_2(t)(e^{i\mathbf{k_2}\mathbf{r}-i\Omega_2 t}\mu_2^+ + e^{-i\mathbf{k_2}\mathbf{r}+i\Omega_2 t}\mu_2^-), \end{aligned} \tag{3.1}$$

where $E_1(t)$ and $E_2(t)$ are the temporal envelopes of the pump and probe pulses, and $\mu_1^+ = \mu|e><g|$ and $\mu_1^- = \mu|g><e|$ are the dipole operators of the pump. The dipole of the probe is chosen to be $\mu_2^+ = \mu|e><g|$ and $\mu_2^- = \mu|g><e|$ for (i) and $\mu_2^+ = \mu|f><e|$ and $\mu_2^- = \mu|e><f|$ for (ii). The electronic transition dipole matrix element μ in general depends weakly on the nuclear coordinate. For simplicity we hereafter neglect that dependence and set $\mu = 1$.

The observable in optical measurements is the polarization defined by

$$P(\mathbf{r},t) \equiv tr\{\mu_2\rho(\mathbf{r},t)\}, \tag{3.2}$$

where $\mu_2 \equiv \mu_2^- + \mu_2^+$ and $\rho(\mathbf{r},t)$ is the total density matrix. Here, tr is the trace operator to obtain the sum of diagonal element. The $\mathbf{r}$ dependence comes through the laser interactions. We next expand the polarization in $\mathbf{k}$ space

$$P(\mathbf{r},t) = \sum_{\mathbf{k}} e^{i\mathbf{k}\mathbf{r}} P_{\mathbf{k}}(t). \tag{3.3}$$

Optical measurements are most commonly carried out using one of the following two detection schemes. First, in homodyne detection one simply measures the outgoing field in a specified direction $\mathbf{k_f}$; (1) $S(t) = |P_{\mathbf{k_f}}(t)|^2$. Second, in the *heterodyne* detection mode, the outgoing field is mixed with a reference field denoted as E_{LO}

(local oscillator), and the signal is given by (2) $S(t) = Im[E_{LO}(\mathbf{k_f}, t)P_{\mathbf{k_f}}(t)]$. Examples of (1) are four-wave mixing and coherent Raman which are observed in the $\mathbf{k_f} = 2\mathbf{k_1} - \mathbf{k_2}$ direction, whereas the pump-probe experiment with $\mathbf{k_f} = \mathbf{k_1} - \mathbf{k_1} + \mathbf{k_2}$ corresponds to the heterodyne detection. In this section, we study the pump-probe spectrum.

We calculate the optical signal to the lowest order of the probe field, $E_2(\mathbf{r}, t)$, but to arbitrary order of the pump field, $E_1(\mathbf{r}, t)$. The probe absorption spectrum is commonly detected by spectrally dispersing the transmitted probe, and the signal is measured as a function of the dispersed frequency ω_2[12]. The dispersed spectrum is given by

$$S[\omega_2] = -2Im\{E_2[\omega_2]P_{\mathbf{k_2}}[\omega_2]\}, \tag{3.4}$$

where

$$E_2[\omega_2] = \frac{1}{\sqrt{2\pi}} \int_{-\infty}^{\infty} dt e^{i\omega_2 t} E_2(t), \tag{3.5}$$

and

$$P_{\mathbf{k_2}}[\omega_2] = \frac{1}{\sqrt{2\pi}} \int_{-\infty}^{\infty} dt e^{i\omega_2 t} P_{\mathbf{k_2}}(t). \tag{3.6}$$

We assume a weak probe and expand the polarization to first order in E_2. The polarization in the $\mathbf{k_2}$ direction is then given by

$$P_{\mathbf{k_2}}(t) = -\frac{i}{2} \int_{-\infty}^{\infty} dt' E_2(t') e^{-i\Omega_2 t'} < [\mu_2^-(t), \mu_2^+(t')] > + c.c., \tag{3.7}$$

where

$$< [\mu_2^-(t), \mu_2^+(t)] > \equiv tr\{[\mu_2^-(t), \mu_2^+(t')]\rho_g\}$$

$$= tr\{\mu_2^- e_{\leftarrow}^{-\frac{i}{\hbar}\int_{t'}^{t} d\tau H_A^0} \mu_2^+ e_{\leftarrow}^{-\frac{i}{\hbar}\int_{-\infty}^{t'} d\tau H_A^0} \rho_g e_{\rightarrow}^{\frac{i}{\hbar}\int_{-\infty}^{t} d\tau H_A^0}\}$$

$$- tr\{\mu_2^- e_{\leftarrow}^{-\frac{i}{\hbar}\int_{-\infty}^{t} d\tau H_A^0} \rho_g e_{\rightarrow}^{\frac{i}{\hbar}\int_{-\infty}^{t'} d\tau H_A^0} \mu_2^+ e_{\rightarrow}^{\frac{i}{\hbar}\int_{t'}^{t} d\tau H_A^0}\}, \quad (3.8)$$

in which the exponential functions with arrows indicate time ordered exponential and $\mu^{\pm}(t)$ are the operators in the interaction picture

$$\mu^{\pm}(t) = e_{\rightarrow}^{\frac{i}{\hbar}\int_{-\infty}^{t} d\tau H_A^0} \mu^{\pm} e_{\leftarrow}^{-\frac{i}{\hbar}\int_{-\infty}^{t} d\tau H_A^0}. \quad (3.9)$$

Here,

$$H_A^0(t) \equiv H_S + E_1(t)(e^{i\mathbf{k}_1\mathbf{r}-i\Omega_1 t}\mu_1^+ + e^{-i\mathbf{k}_1\mathbf{r}+i\Omega_1 t}\mu_1^-). \quad (3.10)$$

The expression Eq. (3.7) together with Eqs. (3.4)-(3.6) is commonly used for a measurement driven by a strong continuous wave (cw) laser. [55, 56, 57]

A. Linear Absorption Spectroscopy

The linear absorption spectrum is a probe absorption without the presence of the pump-pulse. We can obtain the signal only in the case (i), since $|f><e|\rho_g = 0$. Then, by setting $E_1(t) = 0$ in Eq. (3.7) with Eq. (3.10), we have (Fig. 3.2)

$$P_{\mathbf{k}_2}(t) = - \frac{i}{2}\int_{-\infty}^{t} dt' E_2(t') e^{-i\Omega_2 t'}$$

$$\times tr\{\mu_2^- e_{\leftarrow}^{-\frac{i}{\hbar}\int_{t'}^{t} d\tau H_S} \mu_2^+ \rho_g e_{\rightarrow}^{\frac{i}{\hbar}\int_{t'}^{t} d\tau H_S}\} + c.c. \quad (3.11)$$

The correlation function part can be calculated by integrating the Liouville equation

$$\frac{d}{dt}\rho(t) = -\frac{i}{\hbar}[H_S, \rho(t)], \quad (3.12)$$

till time t with the initial condition $\rho(0) = \mu_2^+ \rho_g$ and by taking the element $tr\{\mu_2^- \rho(t)\}$.

B. Probe Absorption for an Arbitrary Shape and Strength of Pump Pulses

Vibrational spectroscopy have proven to be an effective probe of interatomic potentials.[58] In the pump-probe spectroscopy, the pump pulses transfer a small fraction of the ground state distribution to the excited state, thereby creating a "particle" in the excited state and a "hole" in the ground state. The particle and the hole then evolve during the delay period τ, which are detected by the probe absorption signal. It will be convenient in the following calculations to express the spectrum using expectation values rather than a correlation function. This can be done as follows. Let us consider the evolution of the system subject only to the pump field. The Hamiltonian is given by Eq. (3.10) and corresponding solution of Liouville equation is denoted $\rho^0(t)$:

$$\frac{d}{dt}\rho^0(t) = -\frac{i}{\hbar}[H_A^0(t), \rho^0(t)]. \tag{3.13}$$

We next introduce a modified Hamiltonian which includes only the negative frequency component of the probe pulse E_2

$$H_A^{'}(t) \equiv H_A^0(t) + E_2(t)e^{-i\Omega_2 t}\mu_2^+. \tag{3.14}$$

The solution of the Liouville equation with this Hamiltonian will be denoted $\rho'(t)$:

$$\frac{d}{dt}\rho'(t) = -\frac{i}{\hbar}[H_A^{'}(t), \rho'(t)]. \tag{3.15}$$

If we expand $\rho'(t)$ to the first order in the probe, we obtain[59]

$$P_{k_2}(t) \approx 2tr\{\mu_2^-(\rho'(t) - \rho^0(t))\}$$

$$= -i\int_{-\infty}^{t} dt' E_2(t')e^{-i\Omega_2 t'} < [\mu_2^-(t), \mu_2^+(t')] > + \ldots . \qquad (3.16)$$

The above expression agrees with the intensity of the probe absorption. We can thus calculate the probe absorption with the frequency ω_2 by subtracting the solution of $\rho^0(t)$ from that of $\rho'(t)$, which can be expressed in the form

$$S(\omega_2) = -\sqrt{\frac{8}{\pi}} Im\{E_2[\omega_2] \int dt e^{i\omega_2 t} tr[\mu_2^-(\rho'(t) - \rho^0(t))]\}. \qquad (3.17)$$

This scheme can be applied to a system driven by pump pulses of arbitrary number, shape, and strength.

C. Impulsive Pump-Probe Spectroscopy

If the pump and probe pulses are weak and impulsive, we can further simplify the procedures. We expand the correlation function in Eq. (3.16) with respect to the pump interaction. In the case (i), by taking up to the second order in pump interactions, we have

$$\begin{aligned} tr\{[\mu_2^-(t), \mu_2^+(t')]\rho_g\} &= \int_0^t d\tau' \int_0^{\tau'} d\tau'' E_1(\tau')E_1(\tau'')e^{-i\Omega_1(\tau'-\tau'')} \\ &\times \sum_{j=1}^{4} R_j(t, t', \tau', \tau''), \end{aligned} \qquad (3.18)$$

where (Fig. 3.3a-d)

$$\begin{aligned} R_1(t, t', \tau', \tau'') &= tr\{\mu_2^- e_{\leftarrow}^{-\frac{i}{\hbar}\int_{\tau''}^{t} d\tau H_S} \mu_1^+ e_{\leftarrow}^{-\frac{i}{\hbar}\int_{-\infty}^{\tau''} d\tau H_S} \rho_g \\ &\times e_{\rightarrow}^{\frac{i}{\hbar}\int_{-\infty}^{\tau'} d\tau H_S} \mu_1^- e_{\rightarrow}^{\frac{i}{\hbar}\int_{\tau'}^{t'} d\tau H_S} \mu_2^+ e_{\rightarrow}^{\frac{i}{\hbar}\int_{t'}^{t} d\tau H_S}\}, \\ R_2(t, t', \tau', \tau'') &= tr\{\mu_2^- e_{\leftarrow}^{-\frac{i}{\hbar}\int_{\tau'}^{t} d\tau H_S} \mu_1^+ e_{\leftarrow}^{-\frac{i}{\hbar}\int_{-\infty}^{\tau'} d\tau H_S} \rho_g \\ &\times e_{\rightarrow}^{\frac{i}{\hbar}\int_{-\infty}^{\tau''} d\tau H_S} \mu_1^- e_{\rightarrow}^{\frac{i}{\hbar}\int_{\tau''}^{t'} d\tau H_S} \mu_2^+ e_{\rightarrow}^{\frac{i}{\hbar}\int_{t'}^{t} d\tau H_S}\}, \end{aligned}$$

$$
\begin{aligned}
R_3(t,t',\tau',\tau'') &= tr\{\mu_2^- e_{\leftarrow}^{-\frac{i}{\hbar}\int_{t'}^{t} d\tau H_S} \mu_1^+ e_{\leftarrow}^{-\frac{i}{\hbar}\int_{-\infty}^{t'} d\tau H_S} \rho_g \\
&\times e_{\rightarrow}^{\frac{i}{\hbar}\int_{-\infty}^{\tau''} d\tau H_S} \mu_1^- e_{\rightarrow}^{\frac{i}{\hbar}\int_{\tau''}^{\tau'} d\tau H_S} \mu_2^+ e_{\rightarrow}^{\frac{i}{\hbar}\int_{\tau'}^{t} d\tau H_S}\}, \\
R_4(t,t',\tau',\tau'') &= tr\{\mu_2^- e_{\leftarrow}^{-\frac{i}{\hbar}\int_{t'}^{t} d\tau H_S} \mu_2^+ e_{\leftarrow}^{-\frac{i}{\hbar}\int_{\tau'}^{t'} d\tau H_S} \mu_1^- e_{\leftarrow}^{-\frac{i}{\hbar}\int_{\tau''}^{\tau'} d\tau H_S} \mu_1^+ \\
&\times e_{\leftarrow}^{-\frac{i}{\hbar}\int_{-\infty}^{\tau''} d\tau H_S} \rho_g e_{\rightarrow}^{\frac{i}{\hbar}\int_{\infty}^{t} d\tau H_S}\}. \qquad (3.19)
\end{aligned}
$$

Eq. (3.19) is the commonly used description of the response functions for a two-level system[12].

In the case (ii), we have

$$
\begin{aligned}
tr\{[\mu_2^-(t), \mu_2^+(t')]\rho_g\} &= \int_0^t d\tau' \int_0^{\tau} d\tau'' E_1(\tau') E_1(\tau'') e^{-i\Omega_1(\tau'-\tau'')} \\
&\times \sum_{j=3}^{4} R_j'(t,t',\tau',\tau''), \qquad (3.20)
\end{aligned}
$$

where (Fig. 3.4a,b)

$$
\begin{aligned}
R_3(t,t',\tau',\tau'') &= tr\{\mu_2^- e_{\leftarrow}^{-\frac{i}{\hbar}\int_{t'}^{t} d\tau H_S} \mu_2^+ e_{\leftarrow}^{-\frac{i}{\hbar}\int_{\tau''}^{t'} d\tau H_S} \mu_1^+ \\
&\times e_{\leftarrow}^{-\frac{i}{\hbar}\int_{-\infty}^{\tau''} d\tau H_S} \rho_g e_{\rightarrow}^{\frac{i}{\hbar}\int_{-\infty}^{\tau'} d\tau H_S} \mu_1^- e_{\rightarrow}^{\frac{i}{\hbar}\int_{\tau'}^{t} d\tau H_S}\}, \\
R_4(t,t',\tau',\tau'') &= tr\{\mu_2^- e_{\leftarrow}^{-\frac{i}{\hbar}\int_{t'}^{t} d\tau H_S} \mu_2^+ e_{\leftarrow}^{-\frac{i}{\hbar}\int_{\tau'}^{t'} d\tau H_S} \mu_1^+ \\
&\times e_{\leftarrow}^{-\frac{i}{\hbar}\int_{-\infty}^{\tau'} d\tau H_S} \rho_g e_{\rightarrow}^{\frac{i}{\hbar}\int_{-\infty}^{\tau''} d\tau H_S} \mu_1^- e_{\rightarrow}^{\frac{i}{\hbar}\int_{\tau''}^{t} d\tau H_S}\}. \qquad (3.21)
\end{aligned}
$$

In the impulsive limit, the pump and the probe pulses are short compared with the dynamical time scales of the solvent and solute nuclear degrees of freedom. We can therefore make the following assumption,

$$
E_1(t) = \theta_1 \delta(t), \quad E_2(t) = \theta_2 \delta(t-\tau), \qquad (3.22)
$$

where θ_1 and θ_2 are their areas and we take $\theta_1 = \theta_2 = 1$. Then Eq. (3.7) with Eqs. (3.19) or (3.21) reduces to

$$P_{\mathbf{k_2}}(t) = Im\{e^{-i\Omega_2\tau}\sum_{i=1}^{4} R_i(t,\tau)\} \tag{3.23}$$

with (Fig. 3.3e,f)

$$\begin{aligned} R_1(t,\tau) = R_2(t,\tau) &= tr\{\mu_2^- e_{\leftarrow}^{-\frac{i}{\hbar}\int_\tau^t d\tau H_S}\rho_e(\tau)\mu_2^+ \\ &\times e_{\rightarrow}^{\frac{i}{\hbar}\int_\tau^t d\tau H_S}\}, \end{aligned} \tag{3.24}$$

$$\begin{aligned} R_3(t,\tau) = R_4(t,\tau) &= tr\{\mu_2^- e_{\leftarrow}^{-\frac{i}{\hbar}\int_\tau^t d\tau H_S}\mu_2^+\rho_g \\ &\times e_{\rightarrow}^{\frac{i}{\hbar}\int_\tau^t d\tau H_S}\}, \end{aligned} \tag{3.25}$$

or

$$P_{\mathbf{k_2}}(t) = Im\{e^{-i\Omega_2\tau}\sum_{i=1}^{4} R_i'(t,\tau)\} \tag{3.26}$$

with (Fig. 3.4c)

$$\begin{aligned} R_3'(t,\tau) = R_4'(t,\tau) &= tr\{\mu_2^- e_{\leftarrow}^{-\frac{i}{\hbar}\int_\tau^t d\tau H_S}\mu_2^+\rho_e(\tau) \\ &\times e_{\rightarrow}^{\frac{i}{\hbar}\int_\tau^t d\tau H_S}\}, \end{aligned} \tag{3.27}$$

respectively, where

$$\rho_e(\tau) \equiv e_{\leftarrow}^{-\frac{i}{\hbar}\int_0^\tau d\tau H_S}\mu_1^+\rho_g\mu_1^- e_{\rightarrow}^{\frac{i}{\hbar}\int_0^\tau d\tau H_S}. \tag{3.28}$$

In the case (i) $\mu_2^+ = |e><g|$ and $\mu_2^- = |g><e|$, both Eqs. (3.24) and (3.25) contribute to the spectrum. The contribution from Eq. (3.25) does not depend on

the pulse duration τ and coincides with the expectation value in the linear absorption spectrum Eq. (3.11). Thus, we can evaluate it using the same procedure as explained for the linear absorption. The contribution from Eq. (3.24) can be calculated by the following steps; (1) Calculate the initial equilibrium distribution ρ_g. (2) Calculate $\rho_e(t)$ by integrating the Liouville equation (3.12) from $t = 0$ to $t = \tau$ with the initial condition $\rho_e(0) = |e > \rho_g < e|$. (3) Calculate $\rho_{eg}(\tau)$ by integrating the Liouville equation (3.12) from $t = \tau$ to $t = t$ with the initial condition $\rho_{eg}(\tau) = \rho_e \mu_2^+$. The off-diagonal element of density matrix $\rho_{eg}(t)$ agrees with the contribution Eq. (3.24), i.e., $R_1(t, \tau) = R_2(t, \tau) = \rho_{eg}(t)$.

The contribution Eq. (3.27) of (ii) can be calculated from the same procedure as Eq. (3.24) of (i). Once we calculate $P_{\mathbf{k}}(t)$, the probe absorption spectrum is then obtained from Eq. (3.6).

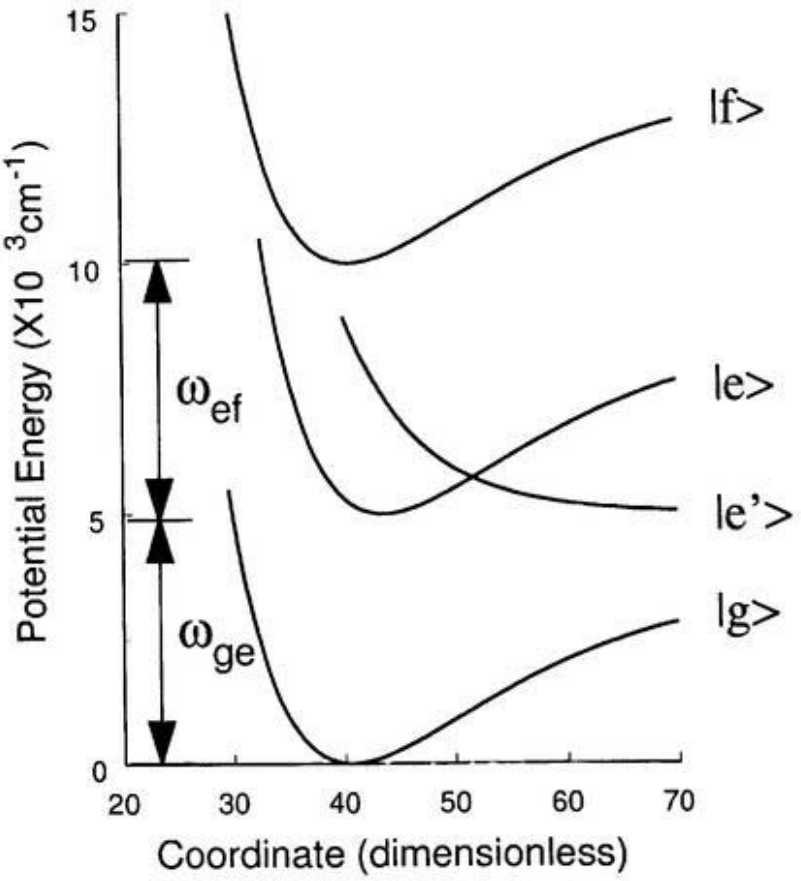

Fig. 3.1. Model potential surfaces of a molecular system. Figure is for a four-level system denoted by $|g>$, $|e>$, $|e'>$ and $|f>$, respectively. The resonant frequency between $|g>$ and $|e>$, and $|e>$ and $|f>$ are, respectively, expressed by ω_{ef} and ω_{ef}.

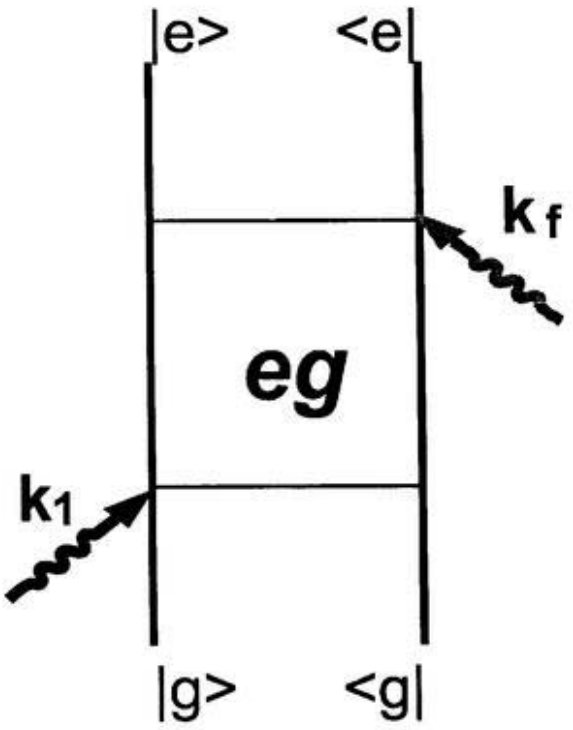

Fig. 3.2. Double-side Feynman diagrams for linear absorption in a two-level system. In a Feynman diagram, the two vertical lines represent the ket and bra of the density matrix. The wavy arrow denotes interactions with the external field. Time increases from bottom to top. The system is initially at thermal equilibrium in the electronic ground state.

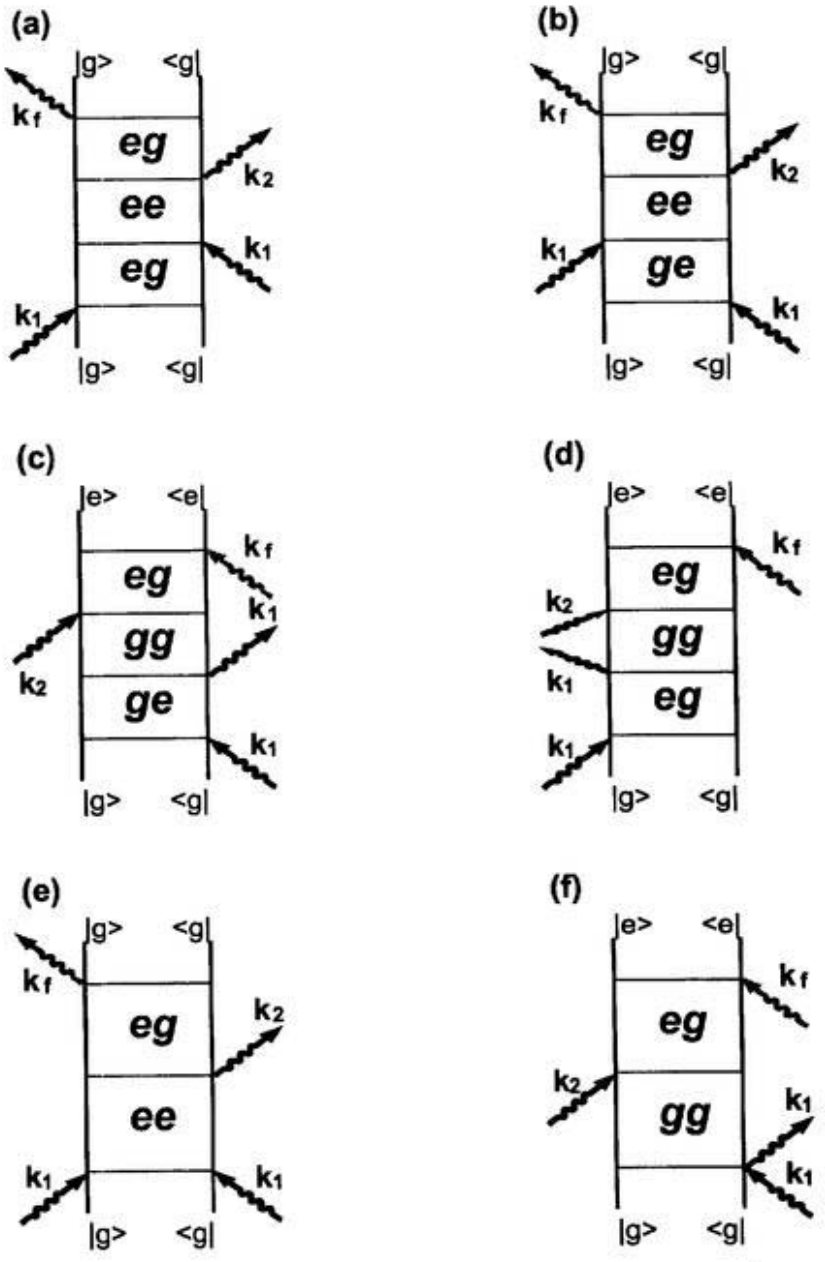

Fig. 3.3. Double-side Feynman diagrams for pump-probe in a two-level system. (a), (b), (c) and (d) denote the response functions R_1, R_2, R_3 and R_4,respectively. (e) and (f) denotes the response functions $R_1 = R_2$and $R_3 = R_4$, respectively, in impulsive limit.

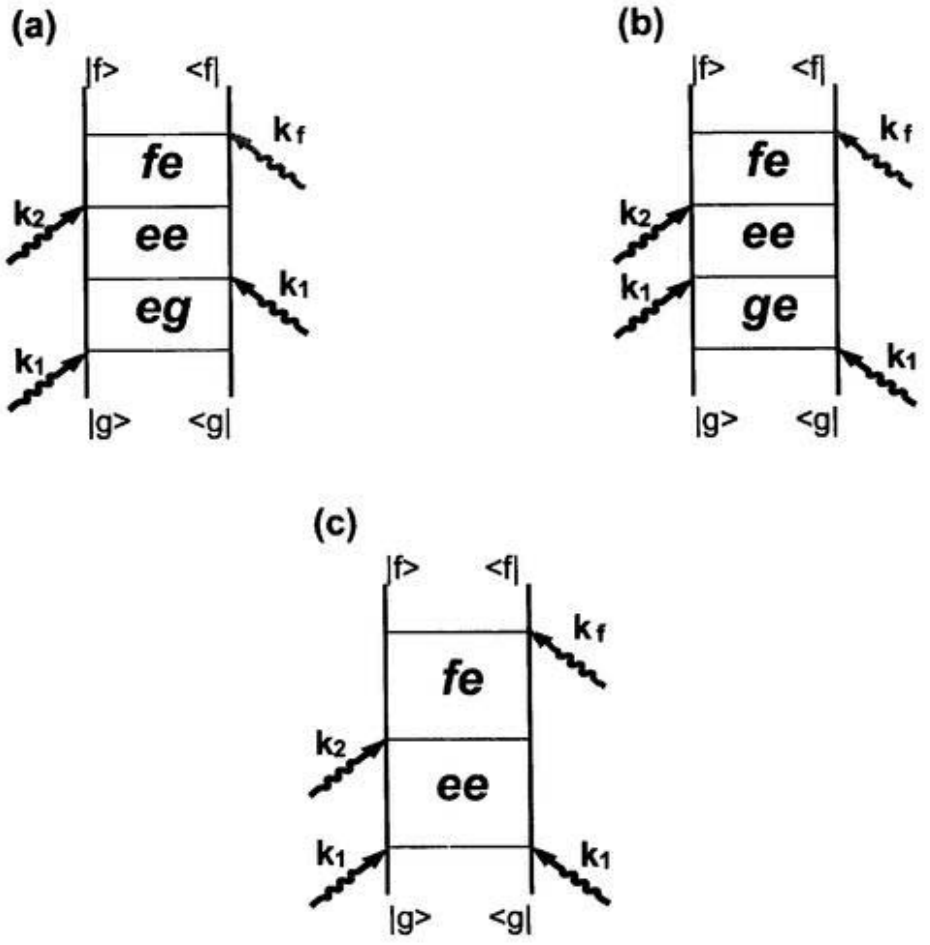

Fig. 3.4. Double-side Feynman diagrams for pump-probe in a three-level system. (a) and (b) denote the response functions R_3' and R_4', respectively. (c) denotes the response function $R_3' = R_4'$ in impulsive limit.

3.2 Impulsive Two-Pulse Photon Echo

In this section, we study a photon echo experiment in a two-level system, which is described by the Hamiltonian (3.1) with $\mu_1 = \mu_2 = \mu$. Beside the pump-probe experiment, the photon echo is another widely used technique for probing dynamical processes in various systems. The photon echo technique can be utilized to eliminate homogeneous broadening selectively, which is in principle impossible using the linear response. We can apply one pulse preparing the system someway, let it evolve freely for a time, apply a second pulse, and then watch the response. If the time between pulses is less than dipole decay time, the polarization will rephase to some extent after additional free evolution. This repahsed polarization emits an "echo" field even in the absence of applied field. Photon echo was named in analogy with the NMR "spin echo".

Invoking the rotating wave approximation the directions of two pulse photon echo are $\pm\mathbf{k_a} = \pm(2\mathbf{k_2} - \mathbf{k_1})$, then the third order nonlinear polarization is given by

$$\begin{aligned} P^{(3)}(t) &= \left(-\frac{i}{\hbar}\right)^3 \int_{-\infty}^{t} dt' \int_{-\infty}^{t'} d\tau' \int_{-\infty}^{\tau'} d\tau'' E_2(t')E_2(\tau')E_1(\tau'') \\ &\times\ e^{-i\Omega_2(t'+\tau')+i\Omega_1\tau''}(R_2''(t,t',\tau',\tau'') + R_3''(t,t',\tau',\tau'')), \end{aligned} \tag{3.29}$$

where (Fig. 3.5a,b)

$$\begin{aligned} R_2(t,t',\tau',\tau'') &= tr\{\mu^- e_{\leftarrow}^{-\frac{i}{\hbar}\int_{\tau'}^{t} d\tau H_S} \mu^+ e_{\leftarrow}^{-\frac{i}{\hbar}\int_{-\infty}^{\tau'} d\tau H_S} \rho_g \\ &\times\ e_{\rightarrow}^{\frac{i}{\hbar}\int_{-\infty}^{\tau''} d\tau H_S} \mu^- e_{\rightarrow}^{\frac{i}{\hbar}\int_{\tau''}^{t'} d\tau H_S} \mu^+ e_{\rightarrow}^{\frac{i}{\hbar}\int_{t'}^{t} d\tau H_S}\}, \\ R_3(t,t',\tau',\tau'') &= tr\{\mu^- e_{\leftarrow}^{-\frac{i}{\hbar}\int_{t'}^{t} d\tau H_S} \mu^+ e_{\leftarrow}^{-\frac{i}{\hbar}\int_{-\infty}^{t'} d\tau H_S} \rho_g \end{aligned}$$

$$\times \quad e_{\rightarrow}^{\frac{i}{\hbar}\int_{-\infty}^{\tau''} d\tau H_S} \mu^- e_{\rightarrow}^{\frac{i}{\hbar}\int_{\tau''}^{\tau'} d\tau H_S} \mu^+ e_{\rightarrow}^{\frac{i}{\hbar}\int_{\tau'}^{t} d\tau H_S} \}. \tag{3.30}$$

In the impulsive limit, the response functions of two pulse photon echo are reduced to (Fig. 3.5c)

$$\begin{aligned} R_2(t,\tau) = R_3(t,\tau) &= tr\{\mu^- e_{\leftarrow}^{-\frac{i}{\hbar}\int_{\tau}^{t} d\tau' H_S} \mu^+ e_{\leftarrow}^{-\frac{i}{\hbar}\int_{0}^{\tau} d\tau' H_S} \rho_g(0)\mu^- \\ &\times \quad e_{\rightarrow}^{\frac{i}{\hbar}\int_{0}^{\tau} d\tau' H_S} \mu^+ e_{\rightarrow}^{\frac{i}{\hbar}\int_{\tau}^{t} d\tau' H_S} \}, \end{aligned} \tag{3.31}$$

where the initial condition is expressed as

$$\rho_g(0) = e_{\leftarrow}^{-\frac{i}{\hbar}\int_{-\infty}^{0} d\tau' H_S} \rho_g e_{\rightarrow}^{\frac{i}{\hbar}\int_{-\infty}^{0} d\tau' H_S}. \tag{3.32}$$

Then the photon echo signal is proportional to the absolute square of a complex-valued electric polarization, $P^{(3)}(t)$:

$$\begin{aligned} S_{IPE} &= |P^{(3)}(t)|^2 \\ &= |R_2(t,\tau) + R_3(t,\tau)|^2. \end{aligned} \tag{3.33}$$

This response function corresponds to the time evolution of molecular system as follows: The first pulse creates a coherence between $|g>$ and $|e>$ states. The total polarization immediately begins to dephase, due to a variety of factors including pure dephasing, inhomogeneous distribution of resonant frequencies, and anharmonicity of vibrational modes. The second pulse arrives at a variable delay time τ, after the first pulse, and interacts twice with the sample and causes a rephasing.

The time evolution of density matrix can be calculated by integrating the Liouville equation (3.12). The contribution from Eq. (3.32) can be calculated by the

following steps; (1) Set the initial equilibrium distribution ρ_g following the procedure described in Sec. 4.1. (2) Calculate ρ_{ge} by integrating the Liouville equation (3.12) from 0 to τ with the initial condition. (3) Operate dipole operators μ^+ to $\rho_{ge}(\tau)$ from left and right sides to obtain $\rho_{eg}(\tau)$. (4) Calculate ρ_{eg} by integrating from τ to $\tau + t$. (5) Take the element of $tr\{\mu\rho_{eg}(\tau + t)\}$.

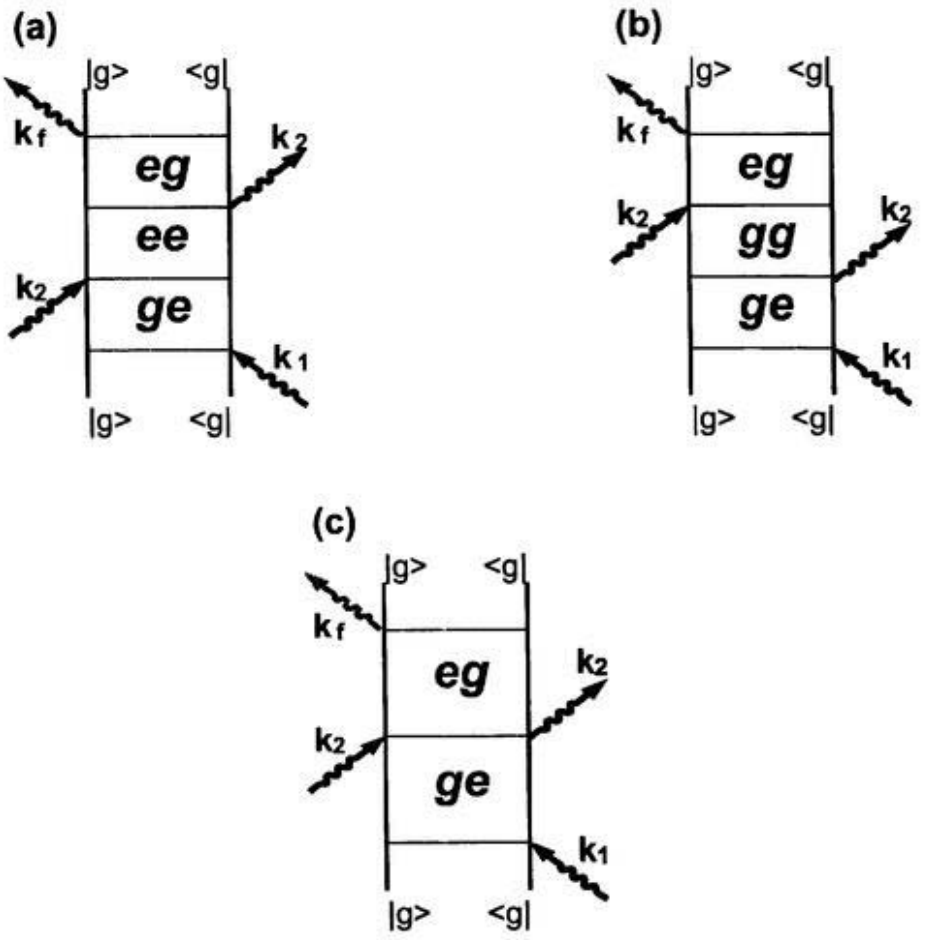

Fig. 3.5. Double-side Feynman diagrams for two-pulse photon echo in a two-level system. (a) and (b) denote the response functions R_2 and R_3, respectively. (c) denotes the response function $R_2 = R_3$ in impulsive limit.

Chapter 4

Numerical Calculation

Y. Tanimura and Y. Maruyama,

"Gaussian-Markovian quantum Fokker-Planck approach to nonlinear spectroscopy of a displaced Morse potentials system: Dissociation, predissociation, and optical Stark effects",

J. Chem. Phys. 107 (1997)1779.

Y. Maruyama and Y. Tanimura,

"Pump-probe spectra and nuclear dynamics for a dissipative molecular system in a strong laser field: predissociation dynamics",

Chem. Phys. Lett. 292 (1998) 28.

4.1 Linear Absorption Spectrum

We consider the displaced Morse potentials system defined by (see Fig. 4.1);

$$\begin{aligned} U_{gg}(R) &= E_e\{1-e^{-a(R-D_1)}\}^2, \\ U_{ee}(R) &= E_e\{1-e^{-a(R-D_2)}\}^2+\hbar\omega_{ge}, \\ U_{ff}(R) &= E_e\{1-e^{-a(R-D_1)}\}^2+\hbar(\omega_{ge}+\omega_{ge}), \end{aligned} \tag{4.1}$$

where E_e, a, and D_j are the dissociation energy, the curvature of the potential, and the displacement, respectively. At the end of next section, we will also include the dissociative state, e' and the diabatic coupling between e and e' described by

$$\begin{aligned} U_{e'e'}(R) &= E_e e^{-2a'(R-D_2)}+\hbar\omega_{ge}, \\ U_{ee'}(R) &= Ae^{-\Delta(R-D_3)^2}. \end{aligned} \tag{4.2}$$

Hereafter, we employ the dimensionless coordinate and momentum defined by $r \equiv R\sqrt{M\omega_0/\hbar}$ and $p \equiv P\sqrt{1/M\hbar\omega_0}$, respectively, where ω_0 is the system characteristic frequency and set as $\omega_0 \equiv \sqrt{U''_{gg}(r)}$. The displacement and curvature of the potential, D_1, D_2, a, etc. are also measured in this unit. We set $E_e = 3649.5[\mathrm{cm}^{-1}]$, $a = 0.6361$, and $D_1 = 40.598(4.64788[\mathrm{A}])$ as the ground state of the Cs_2 molecule[60, 61], which has been studied by a variety of spectroscopic techniques[62, 63, 64, 65]. The fundamental frequency is then given by $\omega_0 = 38.7[\mathrm{cm}^{-1}]$. We calculate linear absorption and pump-probe spectra for various displacement $d \equiv D_2 - D_1$. For the dissociative state, the parameters were chosen to be $a' = 0.6361$, $\Delta = 1.0$, $A = 300[\mathrm{cm}^{-1}]$, and $d' \equiv D_3 - D_1 = 11.09$, respectively. We have used two values

of friction $\zeta = 0.16[\mathrm{cm}^{-1}]$ (weak) and $\zeta = 47.8[\mathrm{cm}^{-1}]$ (strong) and have chosen the inverse correlation time $\gamma = 4.8[\mathrm{cm}^{-1}]$, and the initial temperature $T = 300\mathrm{K}$, which satisfies the condition $\beta\hbar\gamma = \hbar\gamma/k_B T = 0.023 \ll 1$. We first calculate the initial equilibrium state by integrating the equation of motion from time $t = -t_i$ to $t = 0$ with the temporally initial condition,

$$\begin{aligned} W_{gg}^{(0)}(p, r; -t_i) &= \exp[-\beta(\hbar\omega_0 p^2/2 + U_{gg}(r))], \\ W_{gg}^{(n)}(p, r; -t_i) &= 0. \end{aligned} \tag{4.3}$$

Note that Eq. (4.3) is the equilibrium state of the system itself, but, it is not the equilibrium state of the total system including the bath, since it neglects the initial system-bath correlation. In the present formalism, such correlation can be taken into account by the nonzero hierarchy elements, i.e., $W_{jk}^{(n)}(p, r; t) \neq 0$. By integrating the equation of motion from time $t = -t_i$ to $t = 0$, the density matrix comes to the "true" equilibrium state described by the full set of hierarchy $W_{gg}^{(n)}(p, r; t = 0)$, if we set t_i for a sufficiently longer time than the characteristic time of the system. In the following, we use the calculated full set of hierarchy $W_{gg}^{(n)}(p, r; t = 0)$ as the true initial condition. The numerical integrations of these kinetic equations were performed by using second order Runge-Kutta method for finite difference expressions of the momentum and the coordinate space. The size of mesh was chosen to be $30 \times 231 \sim 130 \times 1601$ in the range $-10 < p < 10$ and $34 < r < 57 \sim -34 < p < 34$ and $34 < r < 106$. On each mesh point, the kinetic operator $p\partial W/\partial r$ is approximated by a left-hand difference, $p_i(W(p_i, r_j) - W(p_i, r_{j-1}))/\triangle r$ for $p_i > 0$

and by a right-hand difference $p_i(W(p_i, r_{j+1}) - W(p_i, r_j))/\triangle r$ for $p_i < 0$.[66] The discrete Fourier expression is used for the potential kernel Eq. (2.28). We have taken into account about 11$\sim$24 hierarchy elements for $W^{(n)}$. The accuracy of the calculations was checked by changing the mesh size and the number of terms in the hierarchy.

After obtaining the equilibrium state, we calculate the linear absorption by integrating the equation of motion Eqs. (2.24)-(2.27) instead of the Liouville equation Eq. (3.12) following the procedure explained in Chap. 3.

In Fig. 4.2 we present the linear absorption spectra between the g and e states for different displacements: (a) the small $d = 1$; (b) the intermediate $d = 3$; and (c) the large $d = 7$. Thus, the linear absorption with and without the dissociative state (e' state) give the same result. In each figure, we have calculated two cases of friction $\zeta = 0.16[\text{cm}^{-1}]$ (weak) and $\zeta = 47.8[\text{cm}^{-1}]$ (strong). Since we assumed that probe pulse connect only the g and e states, the contribution of the linear absorption is only from $W_{eg}(p, r; t)$. Here, we set $\triangle\omega = \omega - \omega_{ge}$. Fig. 4.2a is for small displacement. Each peaks represent the transitions between the vibrational levels of the ground and the excited states. Since the Morse potential at the vicinity of potential minimum is well approximated by the harmonic surface, in this small displacement case, the absorption spectra resemble to those from the displaced harmonic oscillator system with the fundamental frequency $\omega_0 = 38.7[\text{cm}^{-1}]$. For $d = 3$, transitions to the higher vibrational levels in the e state can take part in. Thus, we observe many peaks in the weak damping case. Due to the anharmonicity of the potential, the

interval of vibronic lines decreases as frequency increases. In the strong damping case, each vibronic lines are broadened and we simply observe the envelope of the corresponding spectrum. Because the resonant frequency between the ground and excited state is not linear function of coordinate (see Fig. 4.1a) such a displaced harmonic oscillators system, the envelope of peaks is not a symmetric Gaussian in such a way that the blue side of the spectrum is amplified at the expense of the red side. For $d = 7$, the transition mainly occurs between the ground state and continuum dissociative state and the spectrum is widely spread out.[67] The shape of spectra in the weak and strong damping cases are almost identical and overlapped. This is because, in this large displacement case, a laser excitation brings the wavepacket to the continuous dissociative states, where the wavepacket cannot show coherent oscillations.

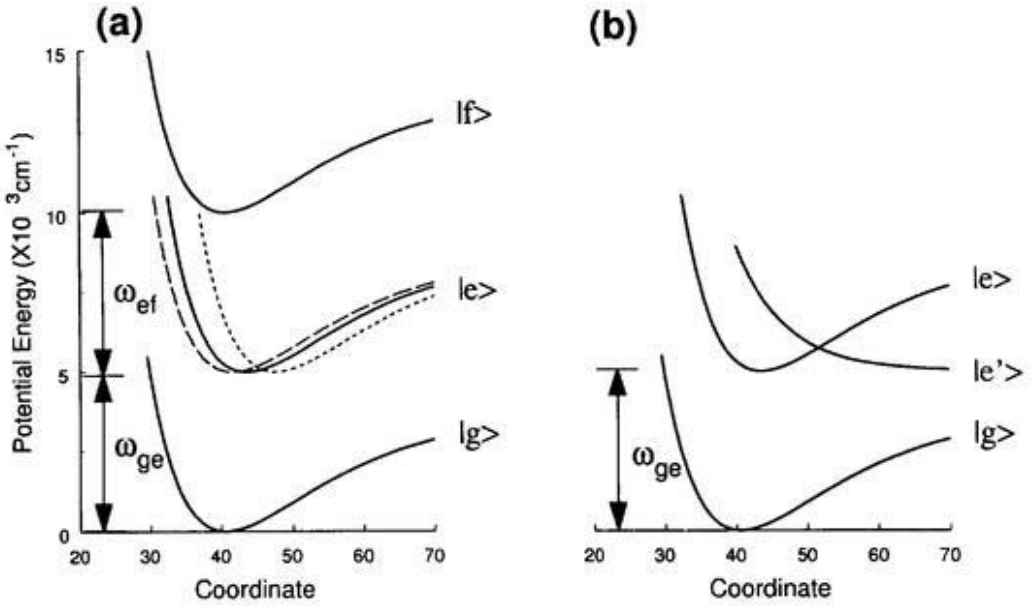

Fig. 4.1. Potential surfaces of the displaced Morse oscillators system. Fig. 4.1a is for a three-level system denoted by $|g>$, $|e>$, and $|f>$, respectively. We display $|e>$ state for three different displacements; $d = 1$(dashed line), $d = 3$(solid line) and $d = 7$(dotted line). The resonant frequency between $|g>$ and $|e>$, and $|e>$ and $|f>$ are, respectively, expressed by ω_{ef} and ω_{ef}. Fig. 4.1b is for a system with the dissociative state ($|e'>$). In this case, we only probe between the $|g>$ and $|e>$ states.

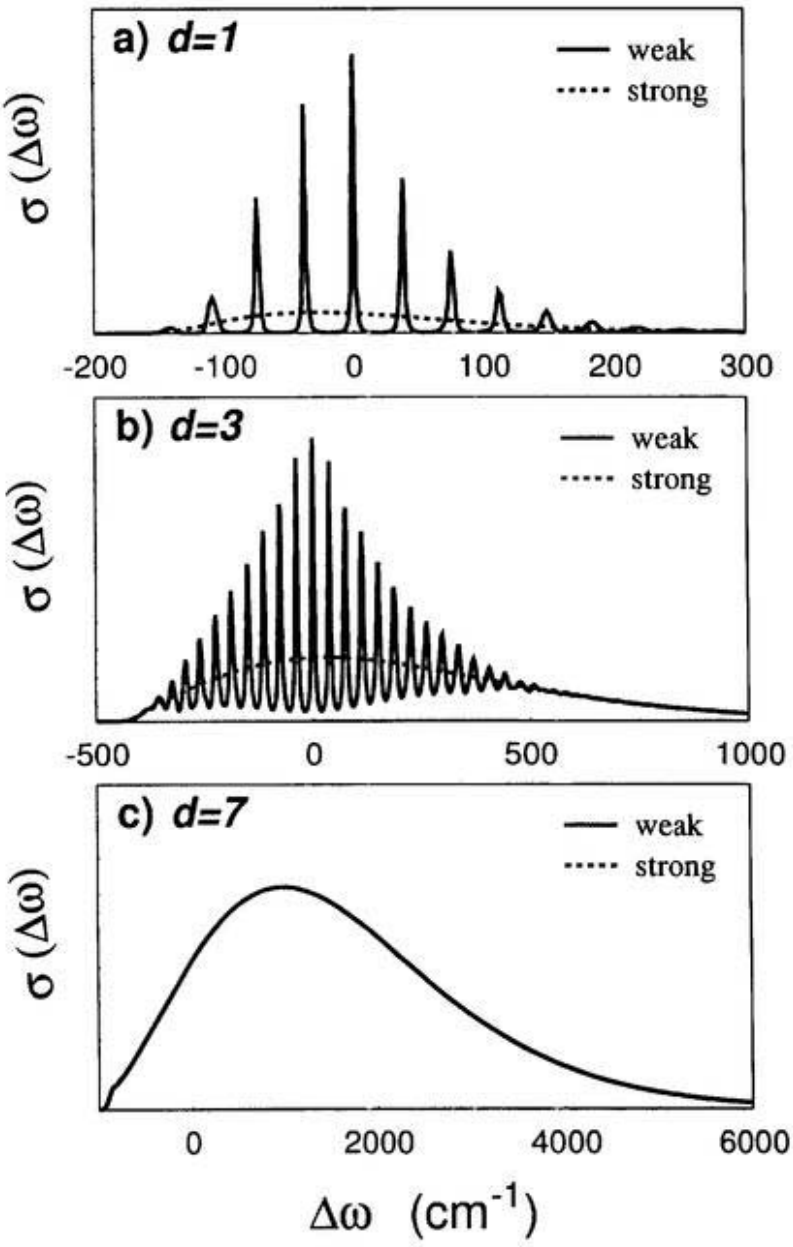

Fig. 4.2. Linear absorption spectra for different displacement. In each figure, we display spectra for the weak damping case (solid line) and the strong damping case(dashed line). Here, we set $\triangle\omega = \omega - \omega_{ge}$.

4.2 Impulsive Pump-Probe Spectrum and Wavepacket Dynamics

Next we present the impulsive pump-probe spectra for various displacement between g and e states as a function of frequency and time. We have carried out the calculations for the weak and strong damping. However, since the difference of them is mostly in the appearance of vibronic lines as seen in Fig. 4.2, hereafter we present the results for the weak damping ($\zeta = 0.16[\mathrm{cm}^{-1}]$) only. We show the result for (i) probe absorption between g and e in Fig. 4.3 and for (ii) the probe absorption between e and f in Fig. 4.4.

We calculated the signal following the procedure explained in Chap. 3 by integrating the equation of motion Eqs. (2.24)-(2.27) instead of the Liouville equation Eq. (3.12). In the case (i), both the particle (Eq. (3.24)) and the hole (Eq. (3.25)) contributes to the signal. Fig. 4.3a shows the spectrum for small displacement $d = 1$. As mentioned in Sec. 4.1, the system is well approximated by the displaced harmonic oscillator, if the displacement is small, and the pump-probe spectrum is therefore similar to the displaced harmonic oscillators case. The height of each peak changes periodically with $T = 1/\omega_0 = 861[\mathrm{fs}]$ corresponding to the coherent motion of the particle created by the pump-pulse. Fig. 4.3b shows the pump-probe spectrum for intermediate displacement $d = 3$. The small peaks in the figure correspond to the vibronic bands as observed in Fig. 4.2b. The envelope of those small peaks reflects the shape of excited wavepacket and the peak of the envelope shows oscil-

lating motion with the period about 1000[fs]. Since the resonant frequency between the ground and excited state ($\delta\omega = [U_{ee}(r) - U_{gg}(r)]/\hbar - \omega_{eg}$) is not a linear function of r, the shape of envelope as a function of $\delta\omega$ is quite different from the original shape of the wavepacket. For instance $\delta\omega$ is a rapidly decreasing function of r in the range $r < \alpha$, where α is about 50 for $d = 3$, but gradually increases for $r > \alpha$ after attained its minimum ($\delta\omega = -380[\mathrm{cm}^{-1}]$ for $d = 3$) at r. Thus, if the wavepacket is in the area of $r < 50$, the envelope corresponding to the wavepacket is broadened and moves quickly, but if the wavepacket is in $r > 50$, the envelope becomes sharp and moves slowly, compared with its actual shape and speed. Fig. 4.3c is for the large displacement $d = 7$. In this case, the kinetic energy of the wavepacket is larger than the dissociation energy and the wavepacket can escape from the potential. Compared with Fig. 4.3b, the highest peak shifts from $-380[\mathrm{cm}^{-1}]$ to $-880[\mathrm{cm}^{-1}]$, since the minimum of $\delta\omega$ now becomes -880 at $r \approx \alpha = 54$ for $d = 7$. Corresponding to the dissociation processes, we have also new peak about $0[\mathrm{cm}^{-1}]$, which agrees with the energy differences between the excited and the ground state at large r.

Fig. 4.4 shows (ii) the probe absorption spectrum between e and f. As explained in Chap. 3, the absorption between e and f is a particle part of (i). Since we fixed the position of the f state just above that of the g state, the displacement between the e and f becomes $-d$. Thus, absorption peaks appear in the opposite direction of $\Delta\omega$ compared with case (i). As seen from Figs. 4.4a-c, we observe the coherent motion of the envelope more clearly than the case of (i), since the spectra of (i) involve the time-dependent particle and the time-independent hole contributions,

whereas the spectra of (ii) involve only the time-dependent particle contribution.

Fig. 4.5 shows the time-evolution of the wavepacket $W_{ee}(p, r; t)$ for intermediate displacement $d = 3.0$ and the weak damping $\zeta = 0.16[\text{cm}^{-1}]$. At time $\tau = 0[\text{ps}]$, the wavepacket with the shape of the ground equilibrium state is created by the pump pulse, then it moves in the positive coordinate direction. At time $\tau = 0.4[\text{ps}]$, the wave packet reaches to the right-hand side of a potential wall and then is bounced back to the negative coordinate direction ($\tau = 0.6[\text{ps}]$). Due to the strong anharmonicity of the potential, distribution functions with different energy have different eigen frequencies. Thus, anharmonic effects lead to a destruction of the initially localized wavepacket as seen in figures at time τ =0.6, 0.8 and 1.0[ps].

Fig. 4.6 shows $W_{ee}(p, r; t)$ for large displacement $d = 7$. In this case, the wavepacket is quickly broken up into small wavepackets because of anharmonicity as explained in Fig. 4.1. The small wavepackets appeared at large r have larger energy and some of them can escape from the potential. This is seen from the figure at time $\tau = 0.6$ - $1.0[\text{ps}]$.

We next show the result with the dissociative state (e' state). Fig. 4.7 is for the intermediate displacement $d = 3$ and the weak damping $\zeta = 0.16[\text{cm}^{-1}]$. Compared with Fig. 4.3b, the peak at $-380[\text{cm}^{-1}]$ and $\tau = 1.4[\text{ps}]$ is noticeably small. This is because the population of wavepacket in the e state decreased after passing the crossing point due to the predissociation process. This can be seen from the time-evolution of the wavepacket shown in Fig. 4.8. In each figure, the upper one is for $|e>$ (the bound state) whereas the lower one is for $|e'>$ (the dissociative state).

Here, we use diabatic representation to display the time-evolution of wavepackets. At $\tau = 0.0$[ps], the wavepacket in the e state moves in the positive coordinate direction. The wavepacket in the e state, then, reaches ($\tau = 0.2$[ps]) and passes ($\tau = 0.4$[ps]) the curve crossing point (about $r = 52$). The transition mainly takes place in the vicinity of the curve crossing point, and the e' population suddenly increases when the e state wavepacket passes the crossing point ($\tau = 0.4$[ps]). This is because we considered the diabatic coupling between e and e' in the localized form (see Eq. (4.2)). After passing the crossing point, the transferred wavepacket starts to move into the e' state potential surface ($\tau = 0.6$[ps]). Since the e' potential is not stable, the wavepacket in the e' state quickly moves to the positive direction and then goes out from the edge of potential ($\tau = 0.8$ and 1.0[ps]).

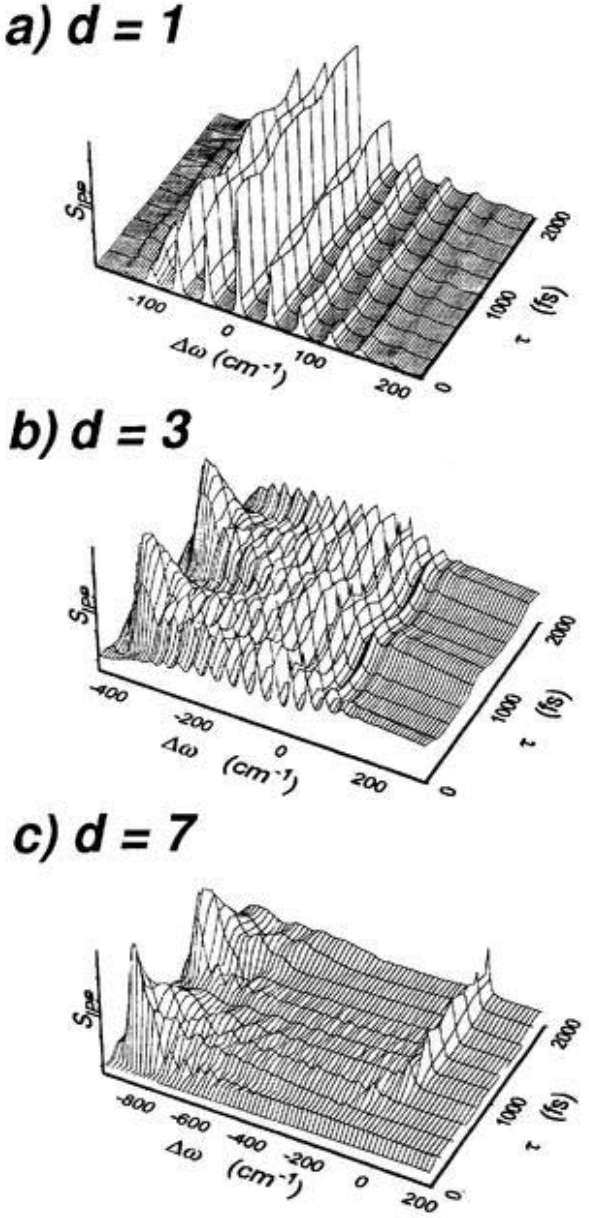

Fig. 4.3. Impulsive pump-probe spectra of three-level system for different displacement in the weak damping case. Here, we probe between the $|g>$ and $|e>$ states. Here, we set $\Delta\omega = \omega - \omega_{ge}$.

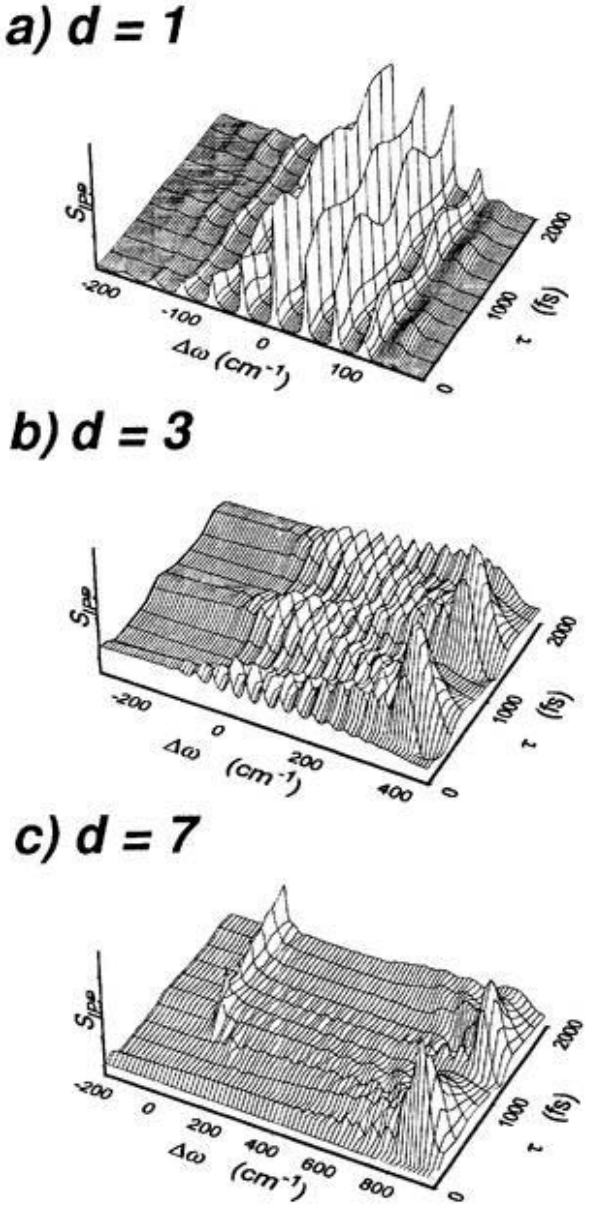

Fig. 4.4. Impulsive pump-probe spectra of three-level system for different displacement in the weak damping case. Here, we probe between the $|e>$ and $|f>$ states and set $\Delta\omega = \omega - \omega_{ge}$.

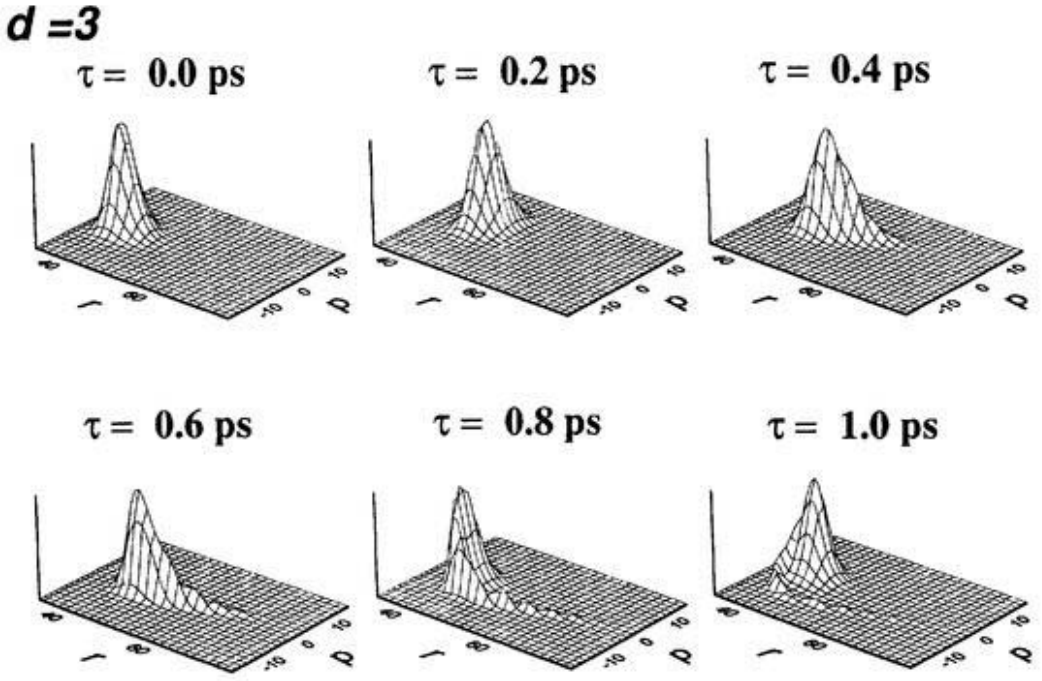

Fig. 4.5. The time-evolution of the wavepacket of the $|e>$ state for the displacement $d = 3$ in the weak damping case.

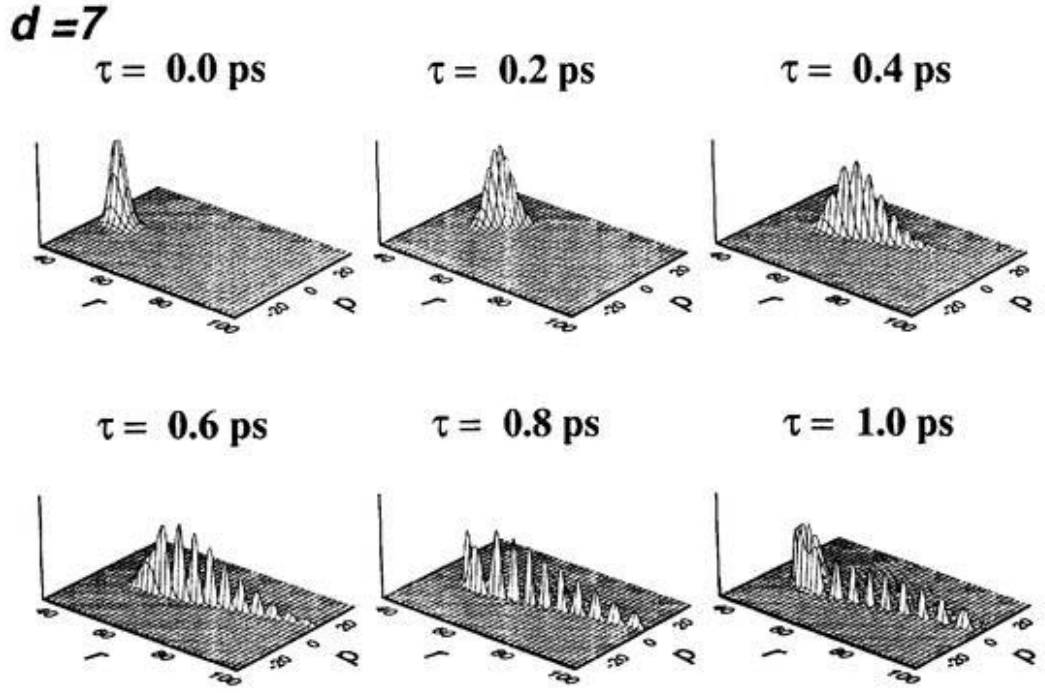

Fig. 4.6. The time-evolution of the wavepacket of the $|e>$ state for the displacement $d = 7$ in the weak damping case.

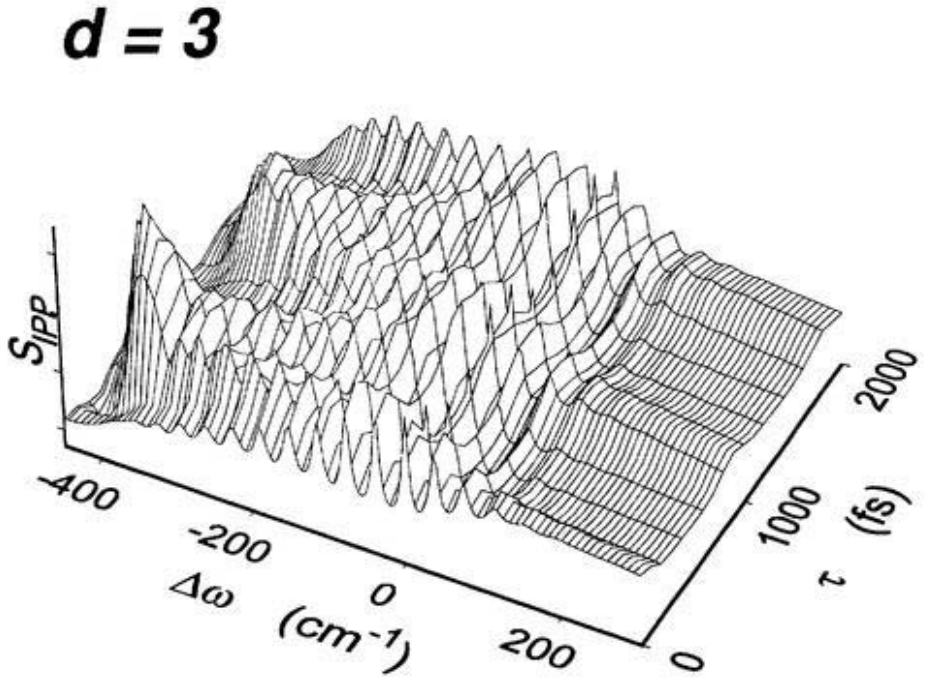

Fig. 4.7. Impulsive pump-probe spectrum of the system with the dissociative state for the displacement $d = 3$ in the weak damping case (see Fig. 4.3). Here, we probe between the $|g>$ and $|e>$ states.

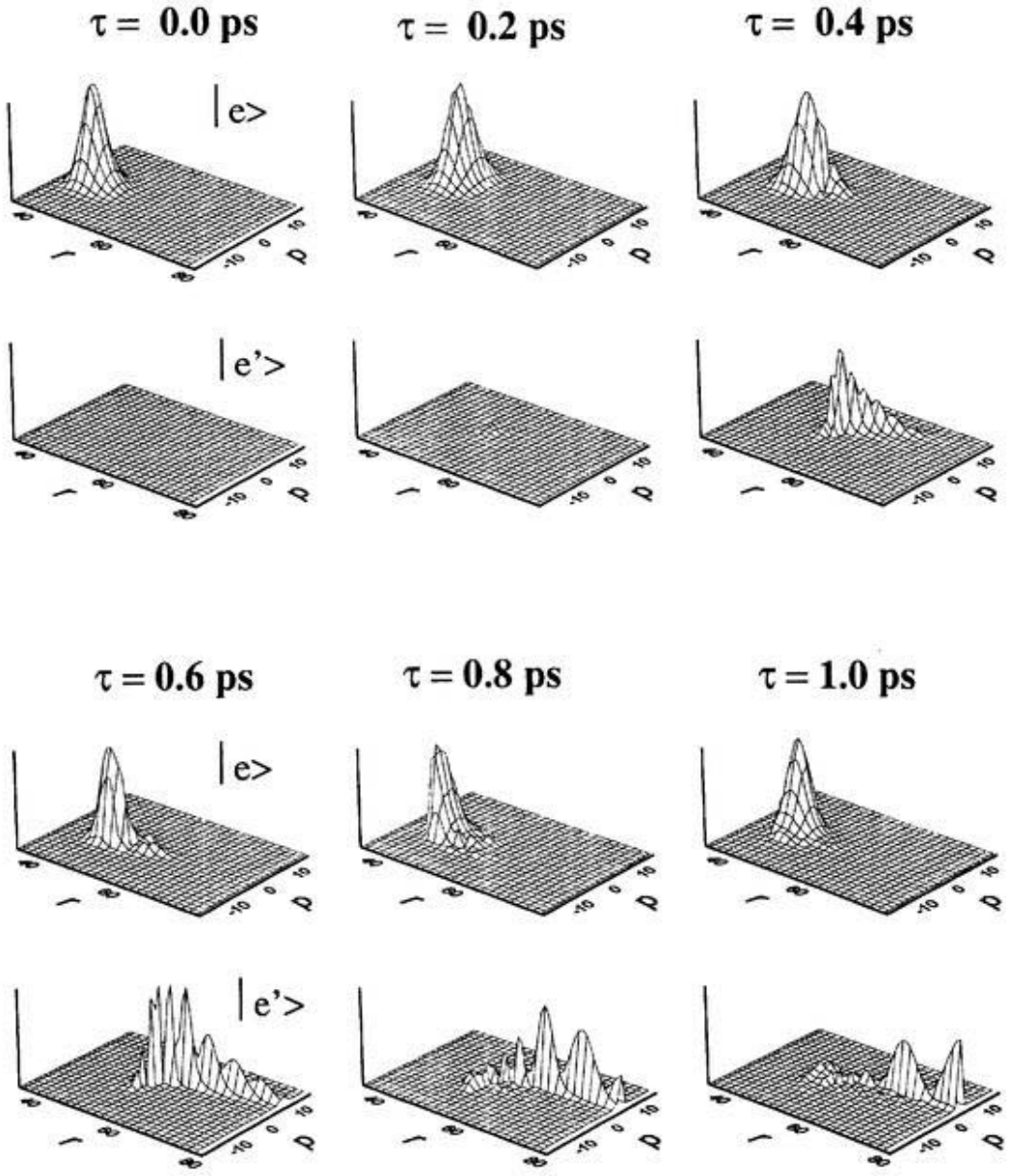

Fig. 4.8. The time-evolution of the wavepacket of the $|e>$ state (the bound state) and $|e'>$ state (the dissociative state) for the displacement $d = 3$ in the weak damping case. In each figure, the upper one is for $|e>$ whereas the lower one is for $|e'>$.

4.3 Probe Absorption for Strong Pump Pulse: Optical Stark Spectroscopy

The present Fokker-Planck equation approach can be applied to a system with any shape of potentials driven by pulses of arbitrary number, shape and strength. Thus, the present approach can generalize the earlier study of optical Stark spectroscopy for a displaced harmonic oscillators system. Following the prescription discussed in Sec. 3.1B, here, we have calculated the pump-probe spectrum for the displaced Morse potential system under a strong pump pulse.

We assume that pump and probe pulses are Gaussian

$$\begin{aligned} E_1(t) &= \theta_1 \exp[-(t/\tau_1)^2], \\ E_2(t) &= \theta_2 \exp[-(t-\tau)^2/\tau_2^2], \end{aligned} \tag{4.4}$$

with resonance central frequencies, i.e., $\Omega_1 = \Omega_2 = \omega_{ge}$. We measure the transition between the $|g>$ and $|e>$ states only. The pulse durations were taken to be τ_1=700[fs] and τ_2=30[fs] and the time delay was varied between τ=−2.0[ps] to τ=1.0[ps], i.e., the pump and the probe pulse are overlapped. The pump intensity was $\mu\theta_1$ = 4.77[THz] and the probe was weak $\mu\theta_2$ = 1.59[GHz]. Considering ideal gas with pressure of 1 [atm] at 300 [K], they are equivalent to 3.14×10^6[W/m^2] and 1.05×10^3[W/m^2], respectively, for the dipole moment μ =1 [Debye]. In this study we have calculated spectra in the case of Fig. 4.1a with intermediate displacement $d = 3$, large displacement $d = 7$ and the predissociation case of Fig. 4.1b for a weak coupling. We choose the constant coupling between excited and dissociative states

in this calculation:

$$U_{ee'}(R) = A.$$

The other parameters were the same as in the impulsive case.

In Fig. 4.9, we show the pump-probe spectrum for the strong pulse excitation. The curve at $\tau = -2.0$[ps] is similar to the linear absorption spectrum (Fig. 4.2b), since the pump is relatively weak and its effects are small at this early stage. The vibronic side-band peaks are observed in the probe absorption spectrum corresponding to various vibronic absorption-emission processes. Due to the anharmonicity of potential and thermal effect, the vibronic transitions yield an asymmetric line shape. The peak about $-380[\text{cm}^{-1}]$ corresponds to the absorption at $\Delta\omega = [U_{ee}(r) - U_{gg}(r)]/\hbar - \omega_{ge} = -380[\text{cm}^{-1}]$ and is attributed to the movement of wavepacket during non-impulsive probe detection. The curves at $\tau = -1.5$ and -1.0[ps] show the dips about 0 $[\text{cm}^{-1}]$ caused by the unbalance between the population and the coherent contribution of absorption spectrum (the coherent dips).[68] When the pump pulse becomes stronger, the coherent dips are broadened. Each vibronic transition shows a Stark splitting whose magnitude is given by the proper Rabi frequency $\Delta\Omega_{nm} = \sqrt{\Delta\omega_{nm}^2 + (\mu E_1(t)/\hbar)^2}$, where $\Delta\omega_{nm}$ is the Rabi frequency between the nth vibrational state of U_g and mth vibrational state of U_e with the energy difference $\Delta\omega_{nm}$. In the early time periods the splitting of the peaks near the center are larger than the side peaks (see curves for $\tau = -1.5$ and -1.0[ps] in Fig. 4.9). This is because the corresponding Rabi frequency $\Delta\Omega_{nm}$ changes signifi-

cantly for small $E_1(t)$ if ω_{nm} is small. The Stark peak of the origin ($\Delta\omega = 0$), which corresponds to zero vibronic line, then splits to the blue and to the red. The Stark shifted peaks of the vibronic side bands can be observed outside of the Stark peaks of the zero vibronic line. In between $\tau = 0.0$ and 1.0[ps], the vibronic mode seems to be decoupled from the optical transition and we observe the spectra similar to the one from the two-level system alone. This can be explained using an argument first employed by Brewer[69, 70, 57]; under strong excitation, the relevant frequency of the molecular system is not ω_{eg} nor ω_0, but rather Rabi frequency $\Delta\Omega_{nm} \approx \mu E_1(t)$, which represents the "dressed" states[71]. For very strong excitation, this frequency is much larger than γ and ω_0. Thus the oscillator cannot respond to the system and the absorption spectrum approaches that of the isolated two-level system. This decoupling at strong fields can potentially be used to eliminate intramolecular vibrational relaxation and to enhance the selectivity of laser induced processes. For $\tau = 1.0$[ps], the pump excitation becomes weak enough and the structure of vibronic bands is recovered.

In Fig. 4.9, the blue Stark shift peak gives an absorptive contribution, whereas the red one gives a gain contribution and becomes negative after $\tau = -0.5$[ps]. In contrast, the Bloch equations or the stochastic Liouville equations predict both peaks to be identical in this resonant excitation case. This phenomenon had been discussed in a study of displaced harmonic oscillator system; Because of the Stark effect, the system has two Stark shifted excited states (dressed states). If the pump field is on resonance, and the temperature of the heat bath is infinite, then the populations of

these two states are the same as predicted by the Bloch or the stochastic Liouville equations. However, if the temperature of the bath is finite, the population of upper Stark level can relax to the lower one which gives a gain of absorption from the lower level to the ground state.

Figure 4.10 shows the probe absorption for a strong pump pulse for the displacement $d = 7$. The spectra are widely spread out, but the peaks at $\Delta\omega = -880[\mathrm{cm}^{-1}]$ are observed outside of the dynamical Stark splitting peaks. The intensity of this peak increased from $\tau = -2.0$[ps] to $\tau = -1.5$[ps], then decreased and reached negative value after $\tau = -1.5$ [ps]. This phenomenon is explained as follows: At the beginning the all population is on g state, the pump pulse transfer the population from g state to e state. When the pump is relatively weak the wavepacket behaves like an impulsive case (Fig. 4.3c), thus the peak at $\Delta\omega = -880[\mathrm{cm}^{-1}]$ is positive and increases with time. When the pump pulse becomes stronger, the population of e state and that of g state become the same with Rabi oscillation. The excited wavepacket is however relaxed to the minimum of the potential, which contribute to the peak at $-880[\mathrm{cm}^{-1}]$ as emission. Then the spectra shows negative peak at $-880[\mathrm{cm}^{-1}]$.

In Fig.4.11, we show the pump-probe spectrum for the strong pulse excitation in the predissociation case. At τ=-1.0[ps] the spectrum shows many peaks in comparison with the non-dissociative case (Fig. 4.9). This is understandable through the following argument. The diabatic coupling between the e and e' states causes the additional vibrational levels to the excited states around the energy at the crossing

point. Since the laser interacts only between the g and e states, such additional levels are dark for the laser excitation. Therefore at the beginning of the pump excitation ($\tau < -1.5$[ps]), these dark levels do not play any role, and the probe absorption in the displaced Morse oscillators (Fig. 4.9) and the displaced Morse oscillators with the dissociative state (Fig. 4.11) show similar results. At time $\tau > -1.0$, when the dissociative state exists, some population in the e state transfers into the dark levels through the diabatic coupling as predissociation. Such reduction of population in the e states induces the additional excitation from the g to e state, which appears as many new peaks in the absorption spectra. For τ=1.0 [ps], the pump excitation becomes weak enough thereby the structure of vibronic bands is recovered.

Fig. 4.12 shows the time-evolution of the wave packet $W_{gg}(p, r; t)$ and $W_{ee}(p, r; t)$ for intermediate displacement $d = 3$. At τ=-1.5[ps] when the pump pulse is weak, the wavepacket is close to the shape of the ground equilibrium state. Since we considered the Gaussian (non impulsive) laser excitation, the wavepacket goes up and down between the ground and excited state potentials through the laser interaction, therefore the shape of the ground state wavepacket is also changed. For $\tau = -0.5$[ps], the population of the excited state increases due to the strong pump pulse, then, for $\tau = 0.0$, 0.5 and 1.0[ps], it slightly decreases and increases because of Rabi flopping. In comparison with the weak excitation case (Fig. 4.5), the wavepacket in the excited state seems to be bounded due to the Stark effects.

In Fig. 4.13, we show the time-evolution of the wave packet $W_{gg}(p, r; t)$ and $W_{ee}(p, r; t)$ for large displacement $d = 7$. In this case the wavepacket on g and

e state are bounded tightly on each potential and the wavepacket on the e state cannot escape from potential by the strong pump pulse.

Figure 4.14 shows the time-evolution of the wavepackets $W_{gg}(p,r;t)$, $W_{ee}(p,r;t)$, and $W_{e'e'}(p,r;t)$ for the predissociation case. In each figure, the upper one is for $|e>$ (the excited state), the middle one is for $|e'>$ (the dissociative state), and the lower one is for $|g>$ (the ground state). For τ=$-$1.0[ps], the population of the excited state increases due to the strong pump pulse, and the population transfer from the g to e state takes place more quickly than that of the case of no dissociative state. The wavepacket created in the e state is forced by the potential to move in the positive coordinate direction. At the $\tau = -0.5$[ps] the wavepacket reaches and passes the curve crossing point (about r=52). Although we have used a constant diabatic coupling, the transition mainly takes place in the vicinity of the curve crossing point, and the e' population suddenly increases when the e state wavepacket passes the crossing point. This is because of the potential difference between e and e' states $\delta U(r) = |U_{ee}(r) - U_{e'e'}(r)|$. The off-diagonal elements $W_{ee'}$ and $W_{e'e}$ are highly oscillatory functions of time at positions far from the curve crossing point, where $\delta U(r)$ is large. Thus, $W_{e'e'}$ can be large only near the crossing point, where $\delta U(r)$ is small.[40] After passing the crossing point, the transferred wavepacket starts to move in the e' state potential surface. Since the e' potential is dissociative, the wavepacket in the e' state quickly moves to the positive direction (τ=$-$0.5[ps]) and then goes out from the edge of potential (τ =0.0 [ps]). In comparison with the bounded case (Fig. 4.12), at τ =0.0[ps], the positive momentum portions of the

wavepackets on g and e are small due to predissociation. For τ =0.0, 0.5 and 1.0 [ps], the populations on g and e states slightly decreases and increases, respectively, and the wavepackets oscillate on each potential surfaces. After the pump pulse vanishes, those wavepackets reach to the thermal equilibrium position of each potential surface after a long time.

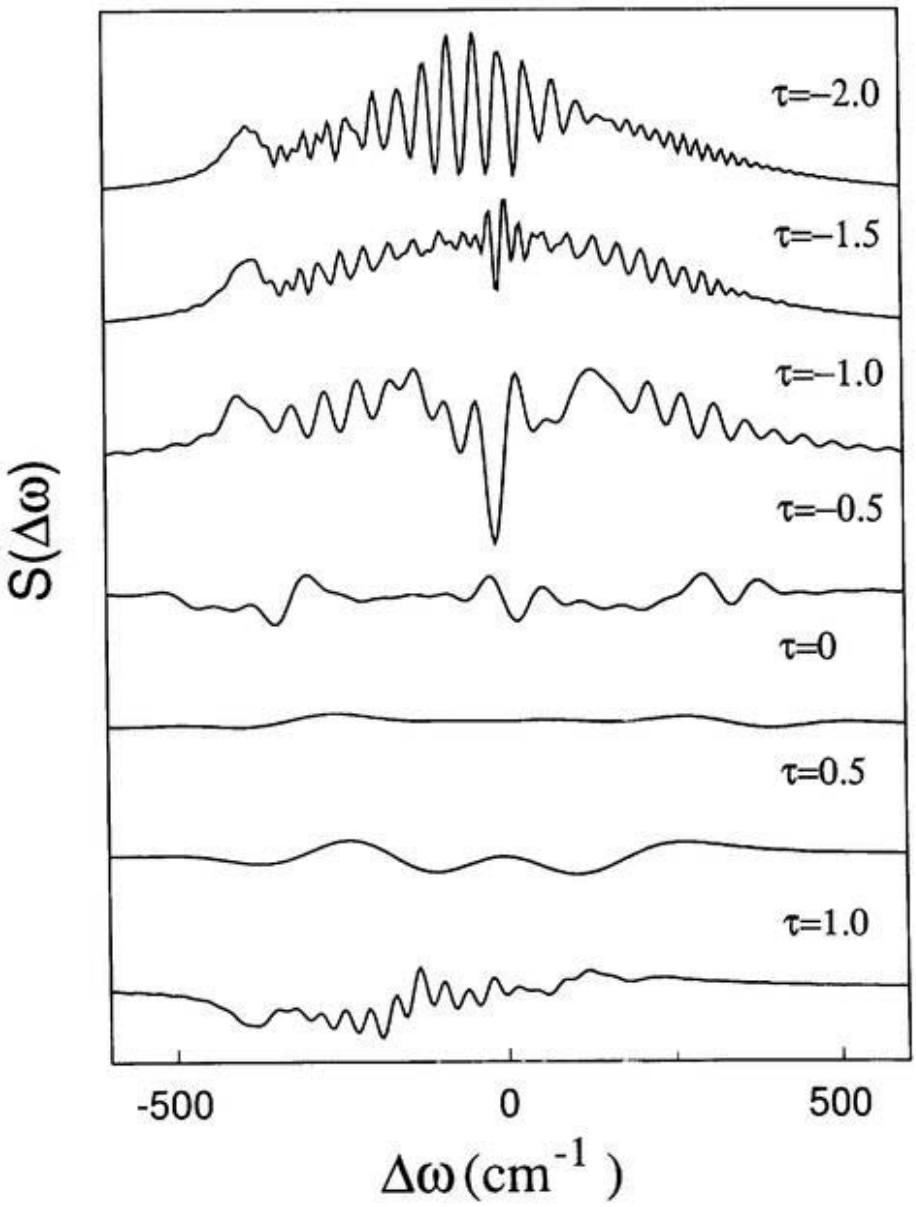

Fig. 4.9. Pump-probe spectrum for a strong excitation ($\mu\theta_1 = 4.77$[THz]) for the displacement $d = 3$. τ denotes pulse delay (ps).

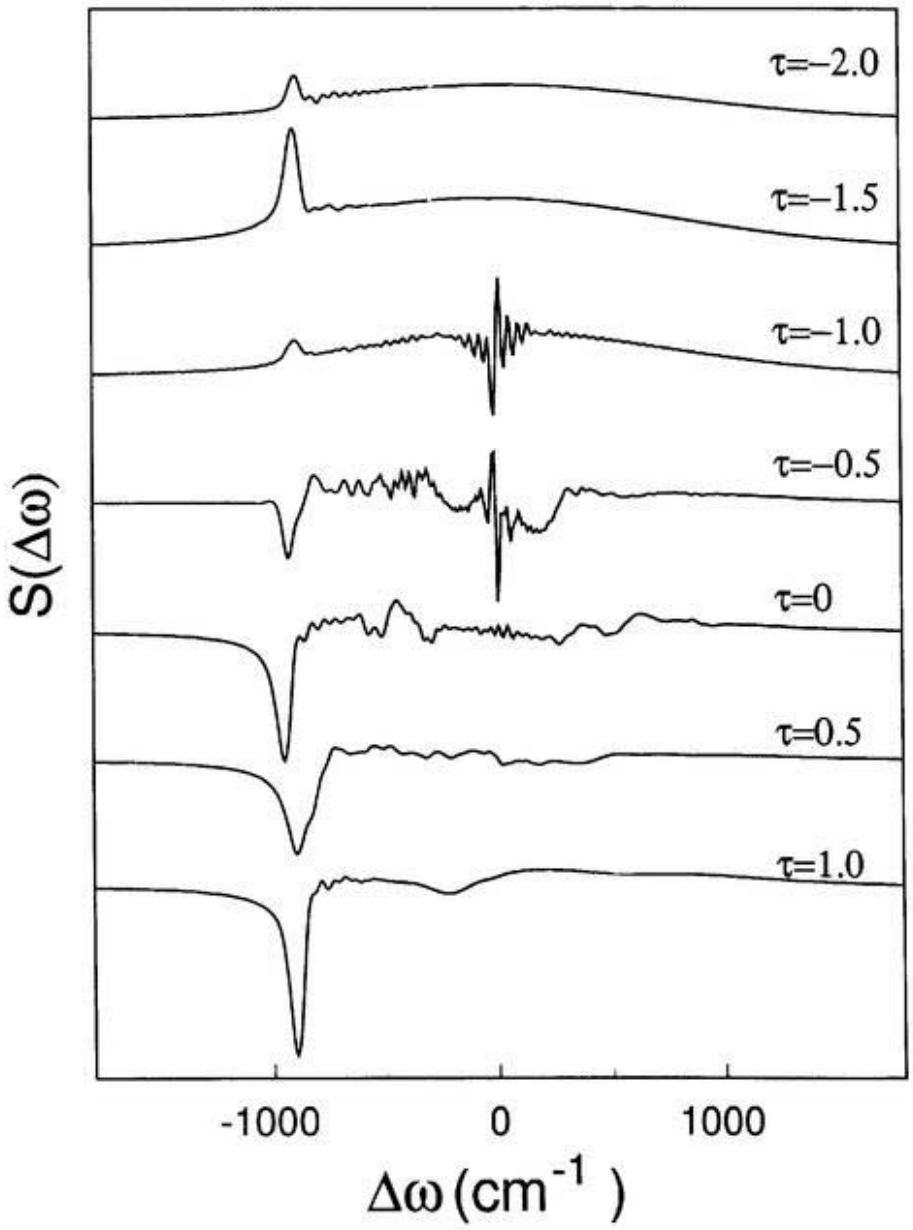

Fig. 4.10. Pump-probe spectrum for a strong excitation ($\mu\theta_1 = 4.77$[THz]) for the displacement $d = 7$. τ denotes pulse delay (ps).

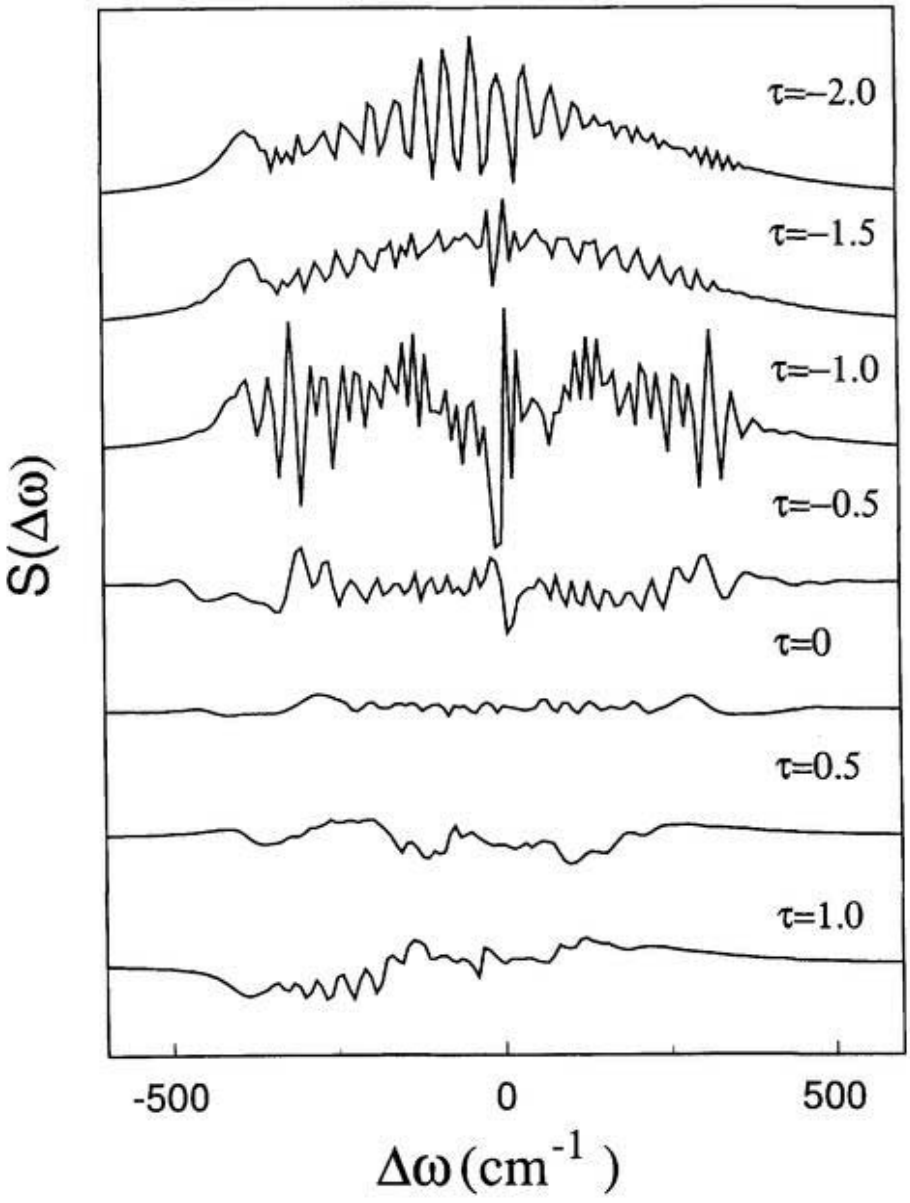

Fig. 4.11. Pump-probe spectrum for a strong excitation ($\mu\theta_1 = 4.77$[THz]) for the displacement $d = 3$ with the diabatic coupling to dissociative state. τ denotes pulse delay (ps).

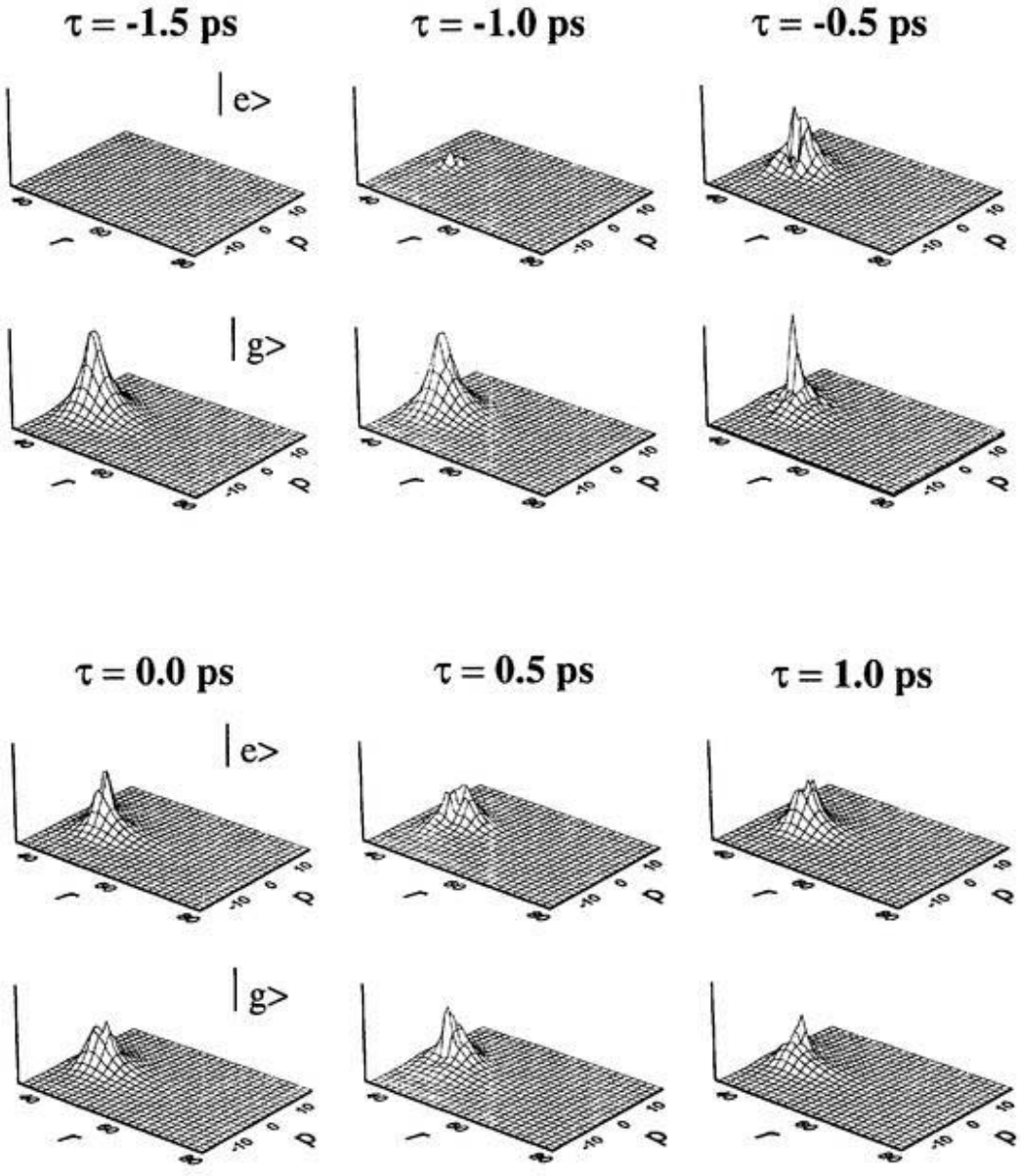

Fig. 4.12. The time-evolution of the wavepacket of the $|g>$ and $|e>$ states for strong pump excitation for the displacement $d = 3$. In each figure, the upper one is for $|e>$ whereas the lower one is for $|g>$. (corresponding to the case of Fig. 4.9)

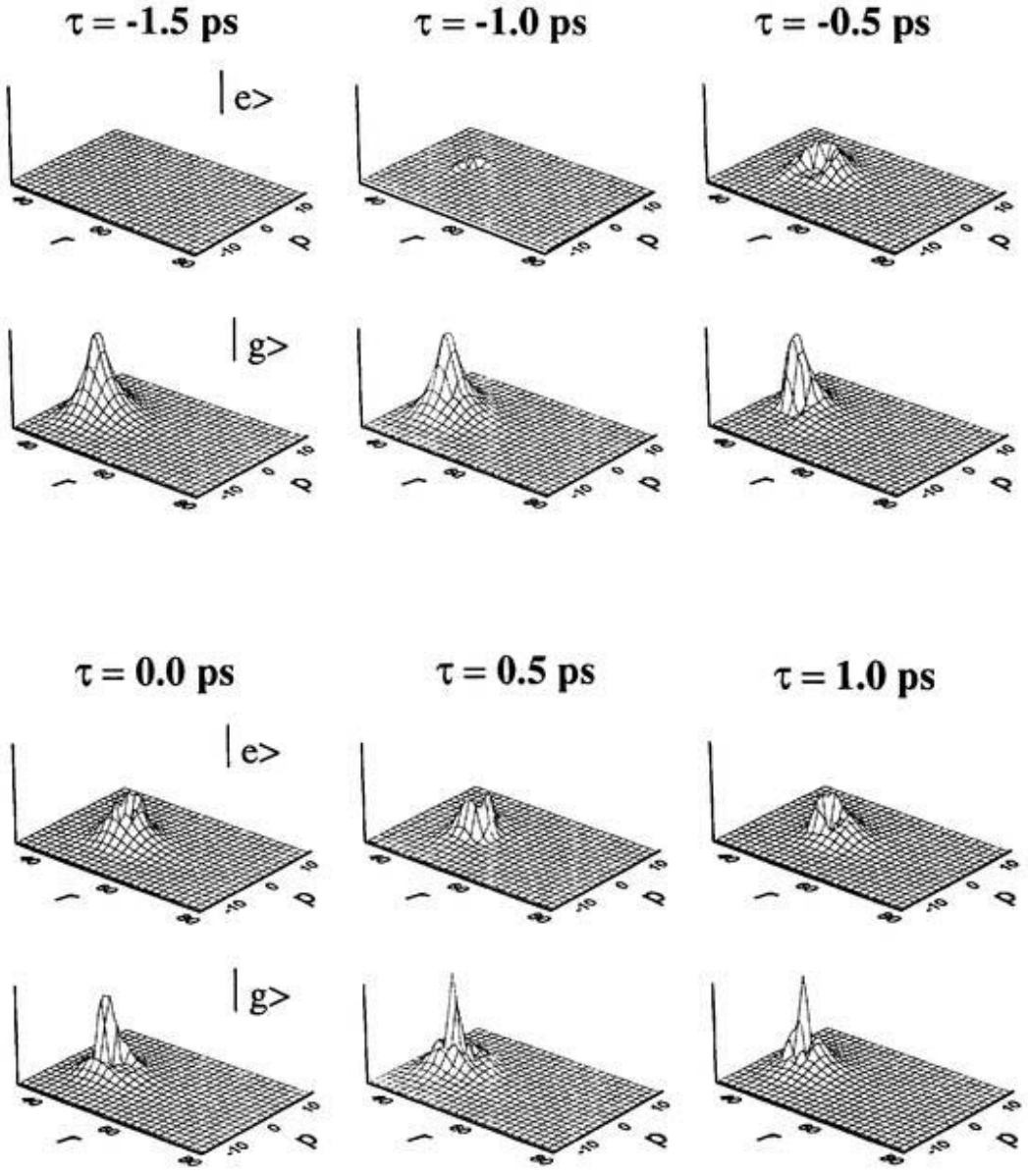

Fig. 4.13. The time-evolution of the wavepacket of the $|g>$ and $|e>$ states for strong pump excitation for the displacement $d = 7$. In each figure, the upper one is for $|e>$ whereas the lower one is for $|g>$. (corresponding to the case of Fig. 4.10)

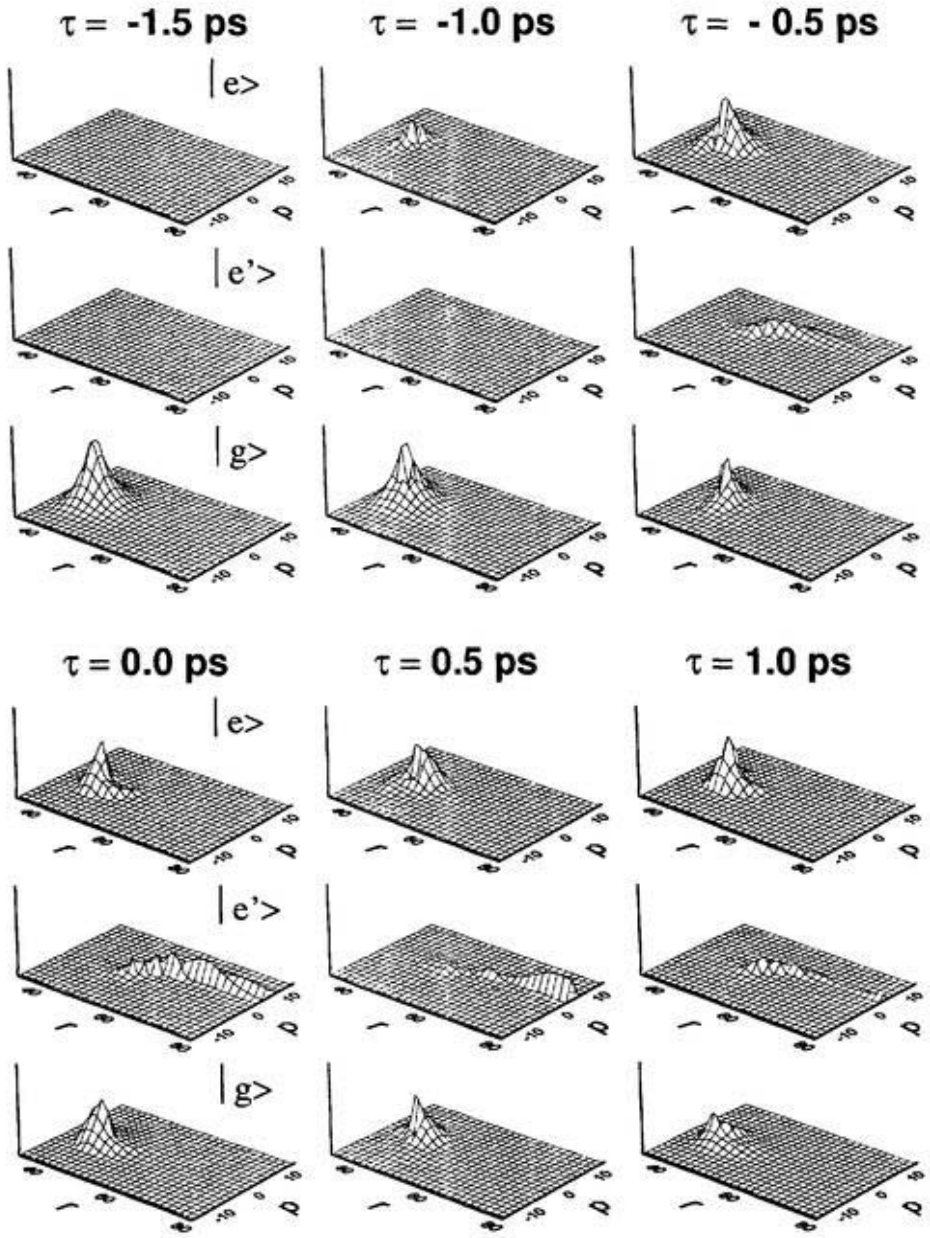

Fig. 4.14. The time-evolution of the wavepacket of the ground ($|g>$), excited ($|e>$) and dissociative ($|e'>$) states for strong pump excitation for the displacement $d = 3$. In each figure, the upper one is for $|e>$, the middle one is for $|e'>$, and the lower one is for $|g>$. (corresponding to the case of Fig. 4.11)

4.4 Impulsive Two-Pulse Photon Echo

In this section we calculate impulsive two-pulse photon echo for a two-level system by using Fokker-Plank equation in the bath coodinate representation. In addition to the Morse potential system, we consider the displaced harmonic system defined by

$$\begin{aligned} U_g(R) &= M\omega_g^2 R^2, \\ U_e(R) &= M\omega_e^2 (R-D)^2 + \hbar\omega_{ge}, \end{aligned} \tag{4.5}$$

where M, ω and D are the mass, frequency and the displacement. We set $\omega_g = \omega_e = 38.7[\mathrm{cm}^{-1}]$ for the case (I) (Fig. 4.15a) and $\omega_g = 38.7[\mathrm{cm}^{-1}]$, $\omega_e = 55.7[\mathrm{cm}^{-1}]$ for the case (II) (Fig. 4.15b). We employed the dimensionless coordinate and momentum defined by $r \equiv R\sqrt{M\omega_0/\hbar}$, $p \equiv P\sqrt{1/M\hbar\omega_0}$ and $q' \equiv q\sqrt{\sigma}$, respectively. Here ω_0 is the system frequency. The displacement and curvature of the potential, d, a, etc. are also used in this unit. The fundamental frequency is then given by $\omega_0 = \omega_g$ in the harmonic systems. In the Morse potential system we set fundamental frequency of Morse potential at minimum is 38.7 $[\mathrm{cm}^{-1}]$. In both cases, the displacement of potentials is set $d = 1.0$. Note that various signals including photon echo for displaced oscillator system with weak anharmonicity have been calculated from responce function approach[16] and have compared with the results from present approach for some special case to check the program. We have used the system-bath coupling $\zeta = 8.0[\mathrm{cm}^{-1}]$ and the inverse correlation time $\gamma = 4.8[\mathrm{cm}^{-1}]$ and its temperature $T = 300\mathrm{K}$, which satisfies the condition $\beta\hbar\gamma = 0.023 \ll 1$ for the cases

(I), (II) and the Morse potential system. In addition, we have used fast modulation noise bath whose inverse correlation time is $\gamma = 48[\mathrm{cm}^{-1}]$ and it satisfies the condition $\beta\hbar\gamma = 0.23 \ll 1$ for the Morse case.

We calculate the signal following the procedure explained in Sec. 3.2. The temporally initial condition is set to be

$$W_{gg}(p, r, q'; -t_i) = e^{-\beta(\hbar\omega_0 p^2/2 + U_{gg}(r))} e^{-q'^2}. \tag{4.6}$$

The grid size was chosen to be $50 \times 201 \times 51$ in the range $-12 < p < 12$, $-10 < r < 10$ and $-5 < q' < 5$ for harmonic displaced system and $60 \times 301 \times 51$ in the range $-15 < p < 15$, $-10 < r < 20$ and $-5 < q' < 5$ for Morse potential system.

First we present the impulsive two pulse photon echo signal for the displaced harmonic potential system. In Fig. 4.16, we display the photon-echo signals as a function of both τ and t. This figure shows absolute value of polarization $|P(\tau, t)|$ though photon echo signal is given by square of polarization. Fig. 4.16a is for the case (I). The free induction decay peak at $\tau = 0$ and $t = 0$ has been cut off for better view the subsequent peaks; it is approximately 11 times higher than that shown in the figure. We see an initial decay followed by oscillations. These are quantum beats, resulting from modulation of the electronic polarization by a vibronic oscillation with frequency $\omega_0 = 38.7[\mathrm{cm}^{-1}]$. This is because $P(\tau, t)$ contains the factor $e^{-i\Delta\omega_{nm}\tau}$, where $\Delta\omega_{nm}$ is the energy difference between the nth vibrational state of U_{gg} and the mth vibrational state of U_{ee}. The photon echo signal corresponds to the peak

along the $\tau = t$ line. The peaks around $(\tau, t) = (860, 0)$, $(0, 860)$, $(1720, 860)$ and $(860, 1720)$[ps] would not be observed if inhomogeneity were present. Fig. 4.16b shows signal for the case (II). The absolute value of polarization is very different. In contrast with the case (I), the peaks are weaker, because the transitions between |g> and |e> have decreased due to the frequency difference of the potential. The peak around (τ, t)=(600, 600) corresponds to the excited state vibration whereas the peak around (860, 860) to the ground state one.

To investigate the effect of bath relaxation time, we calculate the signal for relaxation time of the various bath. Fig. 4.17 shows photon echo signal for the displaced Morse potential system coupled to (a) the slow and (b) the fast modulation bath. For the case (a) the signal is similar to that for the case (I).(Fig. 4.17a) Each peak is broadened, however, because the system has different periods in Morse potential case.

For the case (b) the photon echo signal is very weak because the fast modulation bath destroys the electronic coherence between g and e state quickly.

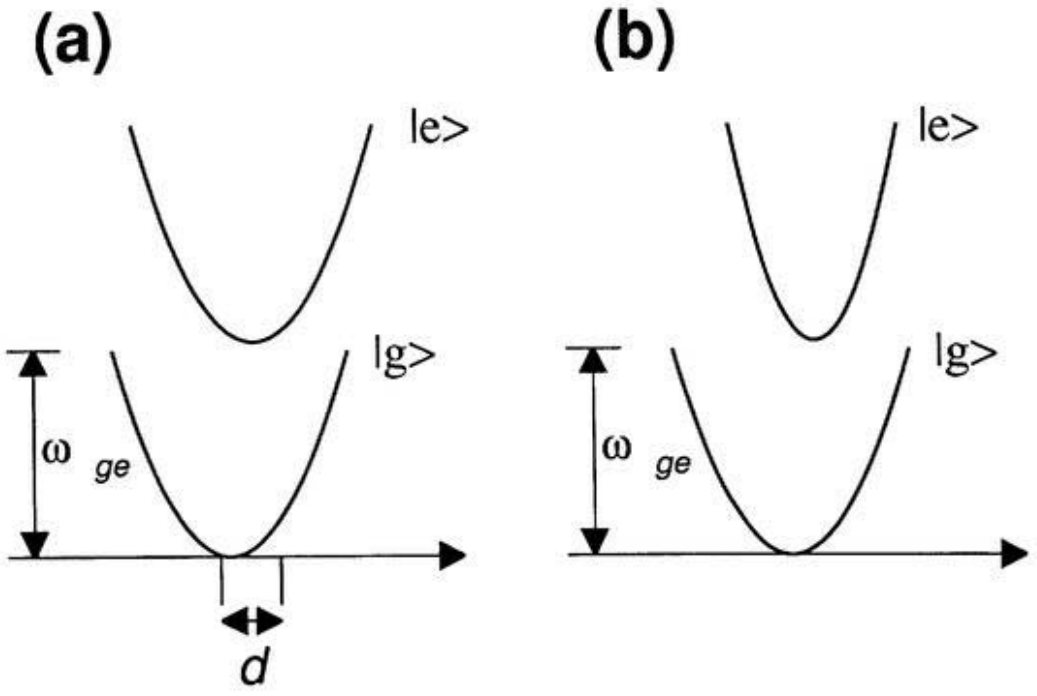

Fig. 4.15. Potential surfaces of the displaced harmonic oscillators system. Fig. 4.15a is for the same frequency case ($\omega_g = \omega_e$). Fig. 4.15b is for the different frequency case ($\omega_g < \omega_e$).

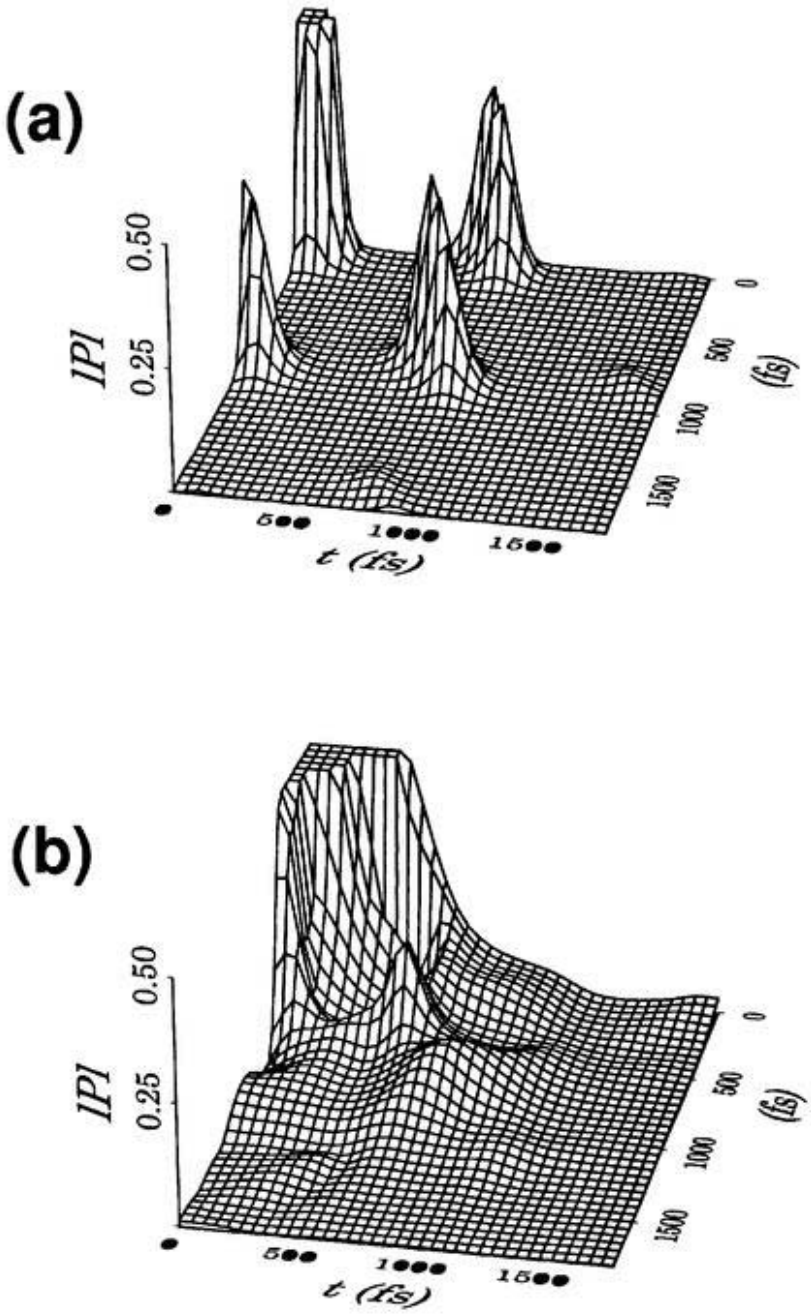

Fig. 4.16. Photon echo signal of the displaced hamonic oscillators system. (a) is for the case (I) ($\omega_g = \omega_e$) and (b) is for the case (II) ($\omega_g < \omega_e$).

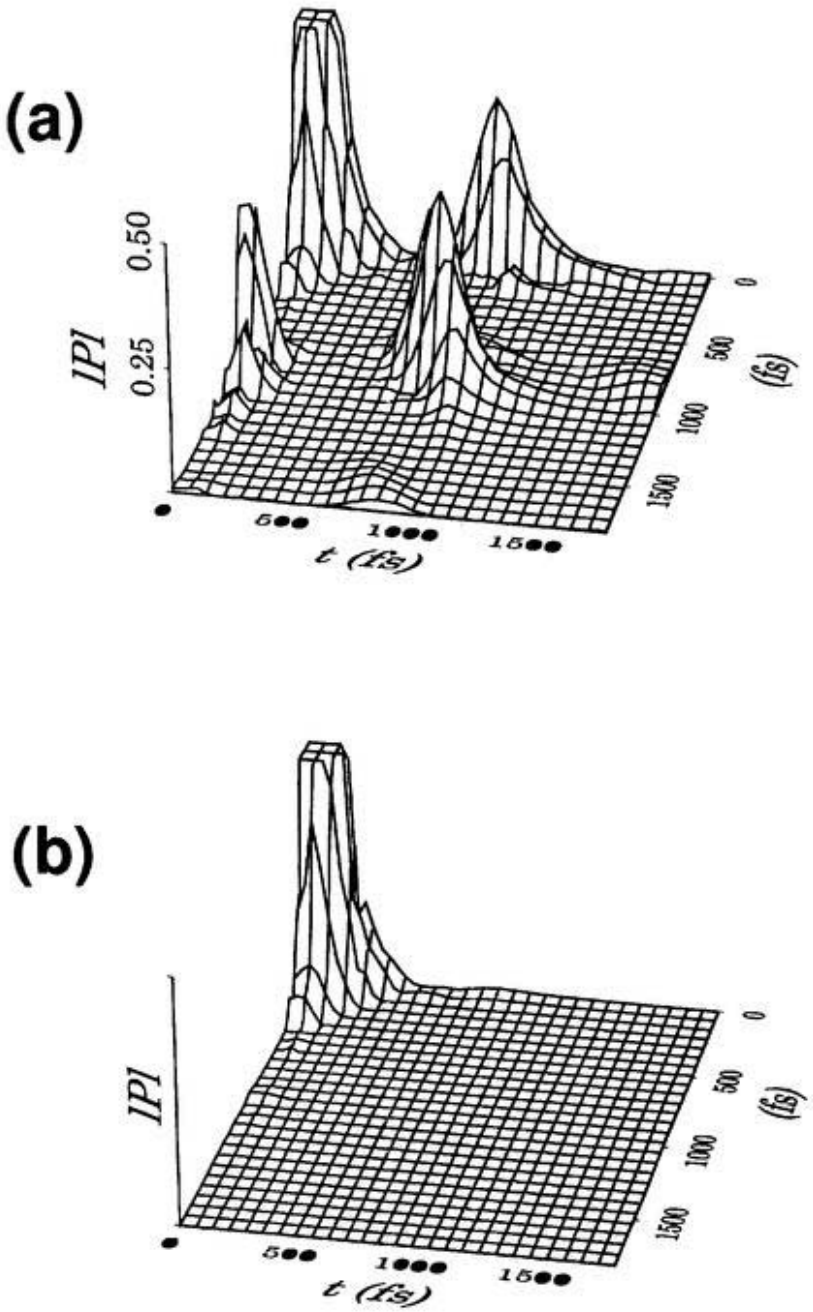

Fig. 4.17. Photon echo signal of displaced Morse oscillators system. (a) is for the slow modulation bath case and (b) is for the fast modulation bath case.

Chapter 5

Conclusion

Quantum activated events, in the absence of dissipation, can be easily studied by a wide variety of numerical methods based on wave function. When dissipation is important, such as liquid phase, wave-function-based methods are not appropriate since dissipation requires the presence of many degree of freedom. Integrating out degrees of freedom leads to a description in terms of equations of motions for reduced density matrices. For a single potential surface, the equation of motion for phase space distribution function is known as the quantum Fokker-Planck equation. The quantum Fokker-Planck equation is generalized to a multistate system with arbitary potentials and a coordinate dependent diabatic coupuling. This approach is applicable for a strong system-bath coupling by introducing a hierarchy of kinetic equations. This equation can also treat wavepacket dynamics at a low temperature heat bath. The present multi-state quantum Fokker-Planck approach provides a powerful means for the study of various chemical processes, where quantum effects play a major role.

In this thesis we have presented a rigorous procedure for calculating the pump-probe spectrum and two-pulse photon echo signal, and calculated the spectra for a displaced Morse oscillators system by using multi-state quantum Fokker-Planck equation for a Gaussian-Markovian bath.

In the dissociation process, we have shown the correspondence between the pump-probe spectrum and the wave packet dynamics. For small displacement, the spectra are similar to those obtained in the displaced harmonic oscillators case. When displacement becomes large, then we observe the movement of wavepacket as

the shift of the envelope of absorption peak. Then for large displacement, we observe the peak corresponding to the dissociation. It is shown that for weak damping, the wavepacket collapses into small packets with different eigen frequencies due to the anharmonicity of the potential.

We have also presented numerical calculations of pump-probe spectra for a strong Gaussian pump pulse. The results show interplay between vibronic transitions and dynamical Stark splitting and the effect of diabatic coupling between bound and dissociative states. In contrast to the results from the conventional Bloch equations which contain an infinite-temperature dephasing, we find that at finite temperatures, the Stark peaks have different heights even when the pump pulse is on resonance. The time evolution of the wavepacket shows the interplay of the predissociation and laser excitation in a dissipative environment.

Therefore the photon echo signals were given for various dissipative systems. The photon echo signal in the different frequency is weaker than that in the same frequency case. In Morse potential case the coherence is lost quickly by the fast modulation bath .

Although in this study we limited our analysis to the system described by the model potential surfaces, it is possible to compare the result of calculation with one of experiments using the realistic potential calculated by ab initio MO or some other method. For example the RISM-SCF can optimize the electronic potential surface of solute including the effect of solvent distribution.[72, 73] Using such a potential surface we can treat solvation dynamics more accuratly.

Furthermore this approach adopt the chirped laser pulse technique. The chirped pulse, which sweeps the frequency of the pulse, is studied theoretically[33, 74, 75, 76, 77, 78, 79] and experimentally[80, 81]. The shape of pulses with a controlled chirp was also recognized for laser chemistry[82, 83], selective optical excitation[84, 85], and the study of optical dynamics[86, 87, 88].

One can also generalize the present approach to study a two-dimensional system, where the interplay between internal energy relaxation with various quantum effects plays an important role. The advent of fast computers equipped with several hundred Megabytes of memory make it possible to study such problems with dissipation. We leave them for future studies.

Bibliography

[1] J. I. Steinfeld, J. S. Francisco, and W. L. Hase, *Chemical Kinetics and Dynamics* (Prentice-Hall, New Jersey, 1989)

[2] R. L. Fork, C. H. B. Cruz, P. C. Becker, and C. V. Shank, Opt. Lett. 12 (1987) 483.

[3] P. Cong, H. Deuel and J. D. Simon, Chem. Phys. Lett. 212 (1993) 367; *ibid.* J. Chem. Phys. 100 (1994) 7855.

[4] H. L. Fragnito, J. -Y. Bigot, P. C. Becker, and C. V. Shank, Chem. Phys. Lett. 160 (1989) 101.

[5] Y. J. Yan and S. Mukamel, Phys. Rev. A41 (1990) 6485; W. B. Bosma, Y. J. Yan, and S. Mukamel, J. Chem. Phys. 93 (1990) 3863.

[6] P. C. Becker, H. L. Fragnito, J. Y. Bigot, C. H. Brito-Cruz, R. L. Fork, and C. V. Shank, Phys. Rev. Lett. 63 (1989) 505; C. J. Bardeen and C. V. Shank, Chem. Phys. Lett. 226 (1994) 310.

[7] M. Cho and G. R. Fleming, J. Chem. Phys. 98 (1994) 3478.

[8] Y. J. Yan and S. Mukamel, J. Chem. Phys. 94 (1991) 179; W. B. Bosma, Y. J. Yan, and S. Mukamel, Phys. Rev. A42 (1990) 6920.

[9] T. Yajima and Y. Taira, J. Phys. Soc. Jpn. 47 (1979) 1620.

[10] E. T. J. Nibbering, D. A. Wiersma, K. Duppen, J. Chem. Phys. 93 (1990) 5477.

[11] Y. J. Yan, L. E. Fried, and S. Mukamel, J. Phys. Chem. 93 (1989) 8149.

[12] S. Mukamel, *Principles of Nonlinear Optical Spectroscopy* (Oxford University Press, New York, 1995).

[13] H. Grabert, P. Schramm, and G. L. Ingold, Phys. Rep. 168 (1988) 115.

[14] B. M. Garraway and K. A. Suominen, Rep. Prog. Phys. 58 (1995) 365.

[15] Y, Tanimura and S. Mukamel, Phys. Rev. E47 (1993) 118.

[16] Y. Tanimura and K. Okumura, J. Chem. Phys. 106 (1997) 2078.

[17] V. Engel and H. Metiu, J. Chem. Phys. 90 (1989) 6116.

[18] R. Kosloff, A. D. Hammerich, and D. Tannor, Phys. Rev. Lett. 69 (1992) 2172.

[19] S. E. Choi and J. C. Light, J. Chem. Phys. 90 (1989) 2593.

[20] S. Mukamel and Y. J. Yan, Acc. Chem. Res. 22 (1989) 301.

[21] J. Cao, M. Messina, and K. R. Wilson, J. Chem. Phys. 106 (1997) 5239.

[22] N. Bloembergen, *Nonlinear Optics* (Benjamin, Boston, 1965).

[23] Y. J. Yan, W. Zhang, and J. Che, J. Chem. Phys. 106 (1997) 2212; J. Che, W. Zhang, and Y. J. Yan, *ibid.* 106 (1997) 6947.

[24] Y. Tanimura and S. Mukamel, J. Chem. Phys. 99 (1993) 9496.

[25] M. Cho and G. R. Fleming, J. Phys. Chem. 98 (1994) 3478.

[26] K. Okumura and Y. Tanimura, Phys. Rev. E53 (1994) 214.

[27] A. H. Zewail, Scienc 242 (1988) 1645.

[28] T. S. Rose, M. J. Rosker, and A. H. Zewail, J. Chem. Phys. 88 (1988) 6672.

[29] L. D. Noodam, A. ten Wolde, A. Lagendijk, and H. B. van Linden van den Heuvell, Phys. Rev. A23 (1981) 236.

[30] S. A. Rice, Science 258 (1992) 412.

[31] P. Brumer and M. Shapiro, Sci. Am. 272 (1995) 34.

[32] M. Sugawara and Y. Fujimura, J. Chem. Phys. 100 (1994) 5646; *ibid.* 101 (1994) 6586; Chem. Phys. 196 (1995) 113.

[33] T. Taneichi, T. Kobayashi, Y. Ohtsuki, Y. Fujimura, Chem. Phys. Lett. 231 (1994) 50.

[34] S. Shi, A. Woody and H. Rabitz, J. Chem. Phys. 88 (1988) 6870.

[35] S. Shi and H. Rabitz, Chem. Phys. 139 (1988) 185; J. Chem. Phys. 92 (1990) 2927.

[36] H. Spohn, Rev. Mod. Phys. 52 (1980) 569.

[37] Y. Tanimura and R. Kubo, J. Phys. Soc. Jpn. 58 (1989) 101.

[38] Y. Tanimura and P. G. Wolynes, Phys. Rev. A43 (1991) 4131.

[39] Y. Tanimura and P. G. Wolynes, J. Chem. Phys. 96 (1992) 8485.

[40] Y. Tanimura and S. Mukamel, J. Chem. Phys. 101 (1994) 3049.

[41] P. W. Atkins, *Physical Chemistry*, 5th ed. (Oxford University Press, Oxford, 1994).

[42] H. Haken and H. C. Wolf, *Molecular Physcs and Elements of Quantum Chemistry* (Springer, New York, 1995).

[43] A. O. Caldeira and A. J. Leggett, Ann. Phys. 149 (1983) 374.

[44] A. O. Caldeira and A. J. Leggett, Physica 121A (1983) 587.

[45] E. Wigner, Phys. Rev. 40 (1932) 749.

[46] R. Kubo, J. Phys. Soc. Jpn. 19 (1964) 2127.

[47] M. Hillery, R. F. O'Connel, M. O. Scully, and E. P. Wigner, Phys. Rep. 106 (1984) 121.

[48] H. W. Lee, Phys. Rep. 259 (1995) 147.

[49] A. M. O. de Almeida, Phys. Rep. 295 (1998) 265.

[50] V. Chemyak and S. Mukamel, J. Chem. Phys. 105 (1996) 4565.

[51] R. Kubo, Adv. Chem. Phys. 15 (1969) 101.

[52] R. F. Loring, Y. J. Yan, and S. Mukamel, J. Chem. Phys. 87 (1987) 5840.

[53] W. T. Pollard, C. H. B. Cruz, C. V. Shank, and R. A. Mathies, J. Chem. Phys. 90 (1989) 199.

[54] P. M. Morse, Phys. Rev. 34 (1929) 57.

[55] B. R. Mollow and M. M. Miller, Ann. Phys. 52 (1969) 464.

[56] P. L. Knight and P. W. Milonni, Phys. Rep. 66 (1980) 21.

[57] H. Tsunetsugu and E. Hanamura, J. Phys. Soc. Jpn. 55 (1986) 3636.

[58] M. Dantus, M. J. Rosker, and A. H. Zewail, J. Chem. Phys. 87 (1987) 2395.

[59] Y. Tanimura and S. Mukamel, J. Phys. Soc. Jpn. 63 (1994) 66.

[60] M. Raab, G. Honing, W. Demetröder, and C. R. Vidal, J. Chem. Phys. 74 (1985) 4370.

[61] W. Weickenmeier, U. Diemer, M. Wahl, M. Raab, W. Demtröder, and W. Müller, J. Chem. Phys. 82 (1985) 5354.

[62] P. Kusch and M. M. Hessel, J. Mol. Spectrosc. 25 (1968) 205; 32 (1969) 181.

[63] E. K. Kraulinya, S. M. Papernov, and M. L. Janson, Chem. Phys. Lett. 63 (1979) 531.

[64] K. Yokoyama, M. Baba, and H. Kato, J. Chem. Phys. 89 (1988) 1209; M. Baba, T. Nakahori, T. Iida, and H. Kato, *ibid.* 93 (1990) 4637; S. Kasahara, Y. Hasui, K. Otsuka, M. Baba, W. Demetröder, and H. Kato, *ibid.* 106 (1997) 4869.

[65] G. Rodriguez and J. G. Eden, Chem. Phys. Lett. 205 (1993) 371; G. Rodriguez, P. C. John, and J. G. Eden, J. Chem. Phys. 103(1995) 10473.

[66] W. R. Frensley, Rev. Mod. Phys. 62 (1990) 745.

[67] R. Schinke, *Photodissociation Dynamics* (Cambrige University Press, Cambridge, 1993).

[68] P. Meystre and M. Sargent III, *Elements of Quantum Optics,* 2nd ed. (Springer, New York, 1991).

[69] A. Schenzle, M. MItsunaga, R. G. DeVoe, and R. G. Brewer, Phys. Rev. A 30 (1984) 325; R. G. DeVoe, and R. G. Brewer, Phys. Rev. Lett. 50 (1983) 1269.

[70] M. Yamanoi and J. H. Eberly, Phys. Rev. Lett. 52 (1984) 1453.

[71] C. Cohen-Tannoudji and S. Haroche, J. Phys. 30 (1969) 123, 153.

[72] S. Ten-no, F. Hirata, and S. Kato, Chem. Phys. Lett. 214 (1993) 391; J. Chem. Phys. 100 (1994) 7443.

[73] H. Sato, F. Hirata, and S. Kato, J. Chem. Phys. 105 (1996) 1546.

[74] K. Duppen, F. de Haan, E. T. J. Nibbering, and D. A. Wiersma, Phys. Rev. A47 (1993) 5120.

[75] B. Amstrup, J. D. Doll, R. A. Sauerbrey, G. Szabó, and A. Lörincz, Phys. Rev. A48 (1993) 3830.

[76] B. Amstrup, G. Szabó, R. A. Sauerbrey, and A. Lörincz, Chem. Phys. 188 (1994) 87.

[77] B. Kohler, J. L. Krause, F. Raksi, K. R. Wilson, V. V. Yakovlev, R. M. Whitnell, and Y. Yan, Acc. Chem. Res. 28 (1995) 133.

[78] J. L. Krause, M. Messina, K. R. Wilson, Y. Yan, J. Phys. Chem. 99 (1995) 13736.

[79] J. Che, M. Messina, K. R. Wilson, V. A. Apkarian, Z. Li, C. C. Martens, R. Zadoyan, and Y. Yan. J. Phys. Chem. 100 (1996) 7873.

[80] B. Kohler, V. V. Yakovlev, J. Che, J. L. Krause, M. Messina, K. R. Wilson, N. Schwentner, R. M. Whitnell, and Y. Yan, Phys. Rev. Lett. 74 (1995) 3360.

[81] H. Petek, A. P. Heberle, W. Nessler, H. Nagano, S. Kubota, S. Matsunami, N. Morita, and S. Ogawa, Phys. Rev. Lett. 79 (1997) 4649.

[82] S. Chelkowski, A. D. Bandrauk, and P. B. Corkum, Phys. Rev. Lett. 65 (1990) 2355.

[83] B. Just, J. Manz, and I. Trisca, Chem. Phys. Lett. 193 (1992) 423.

[84] J. S. Melinger, S. R. Gandhi, A. Hariharan, J. X. Tull, and W. S. Warren, Phys. Rev. Lett. 69 (1992) 2062.

[85] B. Broers, H. B. van Linden van den Heuvell, and L. D. Noordam, Phys. Rev. Lett. 69 (1992) 2062.

[86] T. Tokizaki, Y. Ishida, and T. Yajima, Opt. Comm. 71 (1989) 355.

[87] E. T. J. Nibbering, D. A. Wiersma, and K. Duppen, Phys. Rev. Lett. 68 (1992) 514.

[88] S. Ruhman and R. Kosloff, J. Opt. Soc. Am. B7 (1990) 1748.